Supporting Information

Liquid exfoliation of a series of expanded layered metal-organic frameworks to form nanosheets

Joshua Nicks, Thomas M. Roseveare, Michael Harris, David J. Ashworth, George Danczuk, Lee Brammer and Jonathan A. Foster*

Department of Chemistry, University of Sheffield, Sheffield, S3 7HF, UK

Contents.

S1. Materials and Methods

S1.1. Materials

Commercial solvents, reagents and spectroscopic grade deuterated solvents were used as purchased without further purification, as listed: copper acetate monohydrate (98+%, Alfa Aesar), copper nitrate trihydrate (98%, SLS), 1,4-benzenedicarboxylic acid (99+%, Acros Organics), 1,4-naphthalenedicarboxylic acid (98+%, Alfa Aesar), 2,6-naphthalenedicarboxylic acid (99%, Fluorochem), 4,4'-biphenyldicarboxylic acid (98%, Acros Organics), dimethylformamide (≥99%, Fischer), diethyl ether (≥99.8%, Sigma-Aldrich), acetonitrile (≥99%, Fisher), dimethyl sulfoxide-d_6 (99.5 atom % D, Sigma-Aldrich), deuterium chloride solution (35 wt. % in D2O, ≥99 atom % D, Sigma-Aldrich).

Solvothermal syntheses were carried out using borosilicate vials with Teflon-lined caps in a Carbolite Gero PF 60 Oven. Exfoliations were performed in a Fisher brand Elmasonic P30H ultrasonic bath (2.75 L, 380/350 W, UNSPSC 42281712) filled with water.

S1.2. Analytical Procedures

Laboratory powder X-ray diffraction data were collected using a Bruker-AXS D8 diffractometer using CuK_α (λ = 1.5418 Å) radiation and a LynxEye position sensitive detector in Bragg Brentano para-focussing geometry using a packed glass capillary (MOFs) or a flat zero-background silicon plate (MONs). Synchrotron powder diffraction data (λ = 0.826581) were collected in 0.7mm borosilicate capillaries at beamline I11 at Diamond Light Source using a wide-angle (90 °) position sensitive detector (PSD) comprising 18 Mythen-2 modules.[1,2] A pair of scans related by a 0.25 ° detector offset was collected for each measurement to account for gaps between detector modules. The resulting patterns were summed to give the final pattern for analysis. All data were collected at room temperature.

Elemental microanalyses were performed by the microanalytical service at the Department of Chemistry, University of Sheffield using a Vario MICRO Cube in an atmosphere of pure O_2. Elemental contents are determined to a tolerance of ± 0.5 %.

^{1}H NMR spectra were recorded at 300 K using a Bruker Avance III HD 400 spectrometer equipped with a standard geometry 5mm BBFO probe with a single z-gradient at 400 MHz (1H). MOFs were digested prior to submission, using DCl (5 µL) and d_6-DMSO (1 mL).

Thermogravimetric analyses were performed using a Perkin-Elmer Pyris 1 instrument. Approximately 4 mg of sample was weighed into a ceramic pan, held under nitrogen flow of 20 cm^3 min^{-1} at 25 °C for 10 minutes to purge the sample and allow for equilibration, then ramped to end temperatures at 1 °C min^{-1}. Samples were then held at the final temperature for 10 minutes to allow sample burn off.

FT-IR spectra were recorded using a Perkin Elmer Spectrum 100 FT-IR spectrophotometer, equipped with a SenseIR diamond ATR module. Samples were analysed without further preparation, and spectra were obtained in reflectance mode, using 12 scans with a spectral resolution of 1 cm^{-1}.

SEM samples were loaded onto carbon sticky tab on aluminium sample stubs, coated with approximately 20 nm gold using an Edwards S150B sputter coater and loaded into a TESCAN VEGA3 LMU SEM, operated at 15 keV with images collected at 10,000x magnification using the secondary electron detector.

UV-vis absorption spectra were obtained on a Varian Cary 50 Bio spectrophotometer using standard 1 cm width quartz cells and Perkin Elmer Spectrum One software. Spectral data was formatted using Excel. Colloidal stability was measured qualitatively by eye, observing any aggregation over the course of a month.

Atomic force microscopy images were recorded using a Bruker Multimode 5 Atomic Force Microscope, operating in soft-tapping mode in air under standard ambient temperature and pressure, fitted with Bruker OTESPA-R3 silicon cantilevers operated with a drive amplitude of ~18.70 mV and resonance frequency of ~236 kHz. Samples were prepared by drop-casting 10 µL drops of suspension onto the centre of freshly cleaved mica sheets heated to 100 °C on a hot plate. These sheets were stuck to stainless steel, magnetic Agar scanning probe microscopy specimen discs. Image data were processed using Gwyddion software. For size distribution analysis, particles with lateral dimensions <30 nm were not recorded to neglect defects and small fragments on the sample surface.

Dynamic light scattering measurements collected using a Malvern Zetasizer Nano Series particle size analyser, and a He-Ne laser at 633 nm, operating in backscatter mode (173 °). Samples were equilibrated at 298 K for 30 s prior to analysis.

S2. Crystallographic analysis of the layered MOF series

The syntheses of the layered MOFs Cu(L1), Cu(L2), and Cu(L3) are reported in the experimental section of the main article. This work demonstrates that, upon either exfoliation, activation or solvent exchange, phase transformationxs are observed in the Cu(L1) and Cu(L2) systems as summarised in figure S1. These occur, in part, due to the very properties being exploited when these materials are exfoliated, the weak interlayer forces allowing for a range of different packing motifs with slight differences in layer offset.

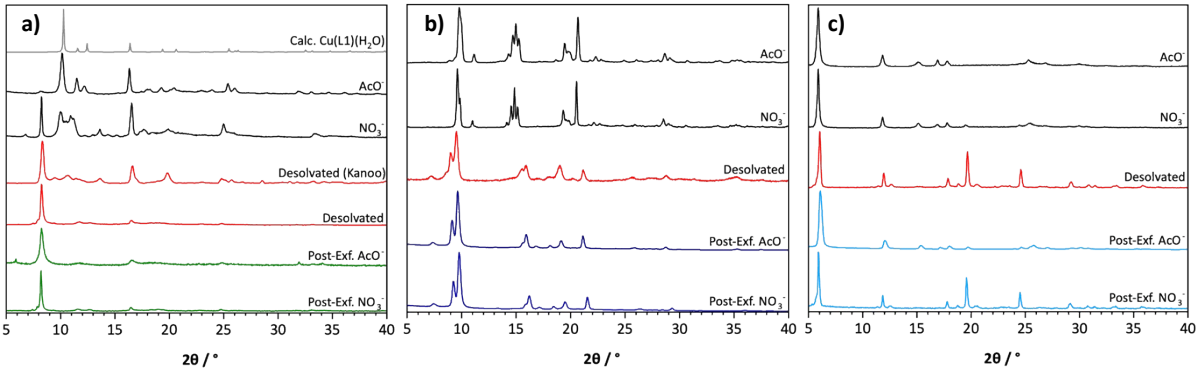

Figure S1. Summary of experimental PXRD patterns obtained for the a) Cu(L1), b) Cu(L2), and c) Cu(L3) MOFs synthesised from the nitrate and acetate solvent (black), desolvated with acetonitrile (red), and obtained post-exfoliation (colour coded to linker). Additional literature patterns are provided for the Cu(L1) system.

In this supplementary section, we provide additional PXRD characterisation and discussion of each material focussed on understanding the phase transformations associated with layer stacking in each material at the synthesis and desolvation stages.

Cu(L1)

Bulk characterisation of the as-synthesised form of **Cu(L1)** revealed a similarity to the structure of **Cu(L1)** previously reported by Kanoo *et al*.[3] However, Pawley refinement analysis[2] using the *TOPAS* software[3,4] showed evidence of a secondary phase (**Figure S2**).

Figure S2. Single-phase Pawley fit of the PXRD pattern of as-synthesised **Cu(L1)**. Unit cell parameters for this (major) phase are consistent with those previously reported by Kanoo *et al.*[3] Peaks not included in the fit are highlighted with black lines. The recorded pattern is shown in blue, the Pawley fit in red and the difference in grey below the fit.

The presence of the minor phase suggests that it is possible to access different stacking arrangements of the coordination layers during the crystallisation of **Cu(L1)**, each of which would give rise to distinct diffraction patterns. It has been concluded that these additional peaks are not due to an impurity, in part, due to the presence of these peaks in subsequent diffraction data of solvent-exchanged, thermally activated or exfoliated samples (Figure S3). Identification of this secondary phase, present both in the as-synthesised form and the solvent-exchanged form was challenging, partly due to data quality and the small number of identifiable peaks of the secondary phase.

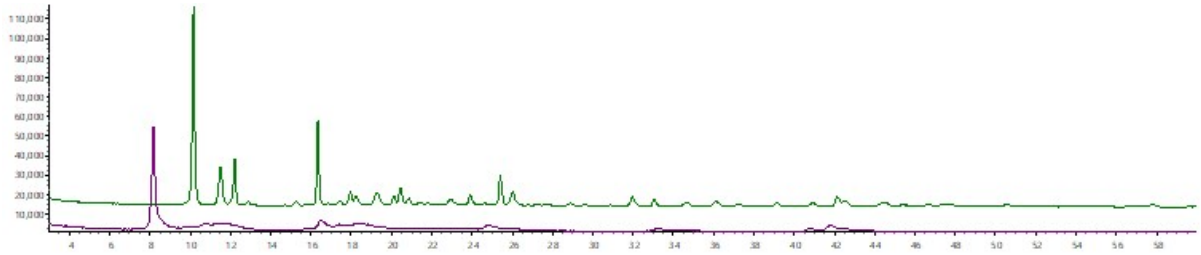

Figure S3. Comparison between **Cu(L1)** as-synthesised in DMF (green) and the subsequent solvent exchanged samples with acetonitrile (purple).

The solvent-exchanged/activated/exfoliated phase can, in turn, be indexed to unit cell parameters consistent with a second **Cu(L1)** phase reported by Kanoo *et al.* (**Figure S4a**).[3] The two reported structures both feature 2D grids constructed from copper paddlewheels and 1,4-naphthalenedicarboxylate but differ in terms of coordinated solvent and the orientation of layers relative to neighbouring ones. The major phase observed in the as-synthesised form (CSD Refcode MAXDEW) features coordinated solvent water and the layers are completely offset, with the copper paddlewheel unit situated above/below the centre of the pore of the neighbouring grid.[3] In the major phase of the solvent-exchanged/activated/exfoliated form (CSD Refcode SUJPAP) neighbouring layers are not fully offset. This second single-crystal structure (CSD Refcode SUJPAP)[3] is an ethanol solvate with coordinated ethanol on the copper paddlewheels. It is unlikely that ethanol is coordinated in the examples reported here, as ethanol was not used, but we suggest that the activation process, either utilising solvent or heating, is sufficient to enable moving of neighbouring layers away from the maximum layer offset observed in MAXDEW.[3]

PXRD data for the as-synthesises and solvent-exchanged/activated materials were fitted by Pawley methods[4] using the *TOPAS* software[5,6] (**Figure S4**). A two-phase fit was used for the as-synthesised form (**Figures S4a and S4c**). The solvent-exchanged/activated material was fitted to a single phase, although data quality made it difficult to confirm the absence of any residual as-synthesised material. Details of the Pawley fits are shown graphically in **Figure S4** with unit cell information in **Table S1**.

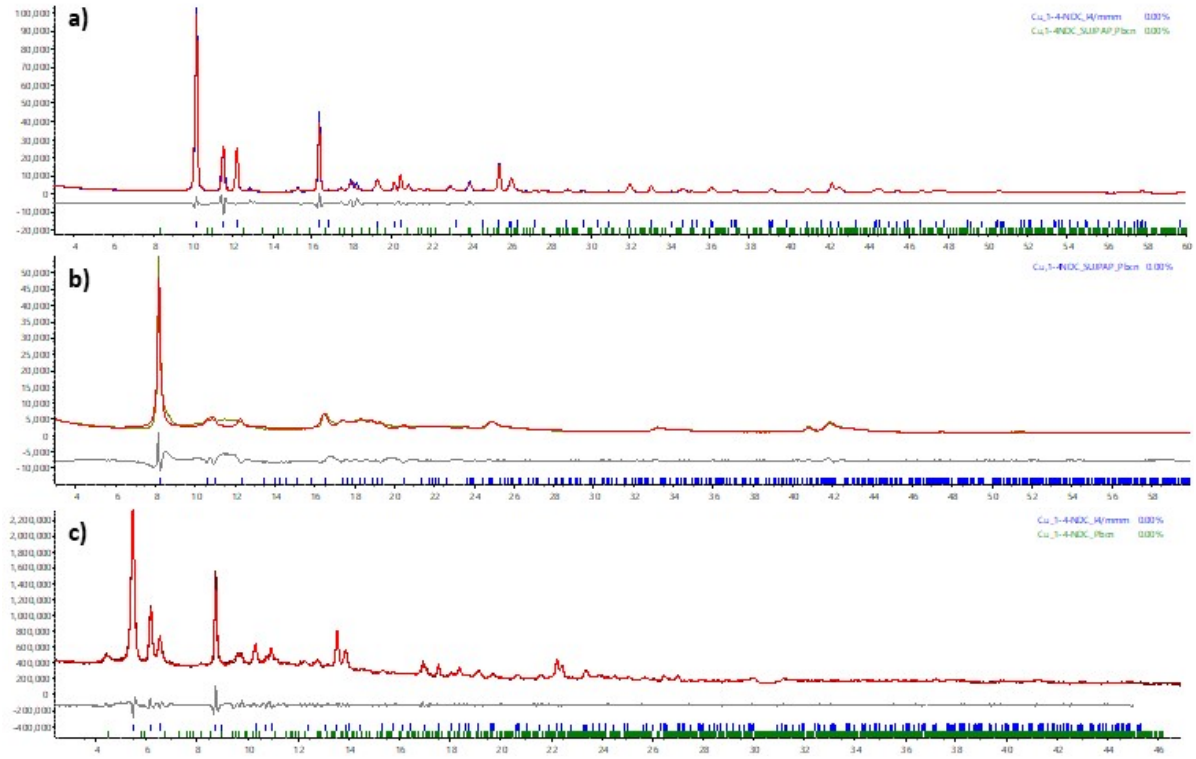

Figure S4. a) Two-phase Pawley refinement of Cu-Kα PXRD pattern of as-synthesised **Cu(L1)** fitted with unit cell parameters similar to MAXDEW (*I*4/*mmm*) as the major phase (blue tick marks) and SUJPAP (*Pbcn*) as the minor phase (green tick marks), both reported as single-crystal structures by Kanoo et al.[3] Pawley refinement, employing 564 parameters (9 background, 1 zero error, 9 peak profile, 5 cell parameters and 540 peaks). **b)** Single-phase Pawley refinement of Cu-Kα PXRD pattern of **Cu(L1)**, following solvent exchange with acetonitrile to enable activation, fitted to unit cell parameters consistent with the crystal structure SUJPAP reported by Kanoo et al.[3] Pawley refinement, employing 462 parameters (9 background, 1 zero error, 5 peak profile, 3 cell parameters and 444 peaks). **c)** Pawley refinement of synchrotron PXRD pattern of as-synthesised **Cu(L1)** fitted with unit cell parameters similar to MAXDEW (*I*4/*mmm*) as the major phase (blue tick marks) and SUJPAP (*Pbcn*) as the minor phase (green tick marks), both reported as single-crystal structures by Kanoo et al.[3] Pawley refinement, employing 1554 parameters (9 background, 1 zero error, 9 peak profile, 5 cell parameters and 1530 peaks).

Table S1. Unit cell parameters obtained from Pawley refinement shown in Figures S4a-c. Synchrotron radiation has a wavelength of λ = 0.826581 Å.

	Radiation	**SG**	**Volume**	***a***	***b***	***c***	***αβγ***	***Rwp***	***Rwp'***
4a	Cu K*α*	*I*4/*mmm*	1700.5(2)	10.8369(5)	10.8369(5)	14.4798(9)	90	0.1052	0.1387
		Pbcn	2989.6(8)	16.171(3)	14.077(2)	13.133(2)	90		
4b	Cu K*α*	*Pbcn*	3031(3)	16.104(8)	14.340(8)	13.123(8)	90	0.1352	0.0650
4c	Synchrotron	*I*4/*mmm*	1706.8(2)	10.8445(3)	10.8445(3)	14.5132(9)	90	0.0330	0.0697
		Pbcn	2950.9(5)	15.945(1)	14.168(1)	13.063(1)	90		

Cu(L2)

Similar to the L1 analogue there are several examples of two-dimensional coordination polymers constructed of paddlewheel secondary building units and 2,6-naphthalenedicarboxylates,[8–10] including single-crystal structures of a 2D paddlewheel grids Zn(L2) DMF solvates.[8,9] The calculated powder patterns of Zn(L2)-DMF, however, do not match the observed powder patterns when a copper analogue is synthesised. Indexing and Pawley fitting the PXRD pattern of as-synthesised **Cu(L2)**, however, gave unit cell dimensions comparable to a previously reported 2D zinc-PW coordination polymer (**Figure S5a**) with axial lutidine ligands,[10] whose crystal structure was determined from PXRD data (Refcode: XOLZUT).

As was observed with solvent-exchange/activation/exfoliation of **Cu(L1)**, the **Cu(L2)** analogue also exhibits a phase transformation under similar conditions. Pawley fitting of its PXRD pattern shows that the phase transformation observed for **Cu(L2)** results in a phase with unit cell dimensions similar to a [Cu(L2)(py)] 2D PW coordination polymer (Refcode: XOMBAC) reported in the same article as the [Zn(L2)(lutidine)] phase (Refcode: XOLZUT).[10] As we observed when studying **Cu(L1)**, evidence of the residual amounts of original phase (*cf*. Refcode: XOLZUT) can be seen, suggesting weak interlayer interactions leading to easy layer-layer dislocation. Details of the Pawley fits are shown graphically in **Figure S5** with unit cell information in **Table S2**.

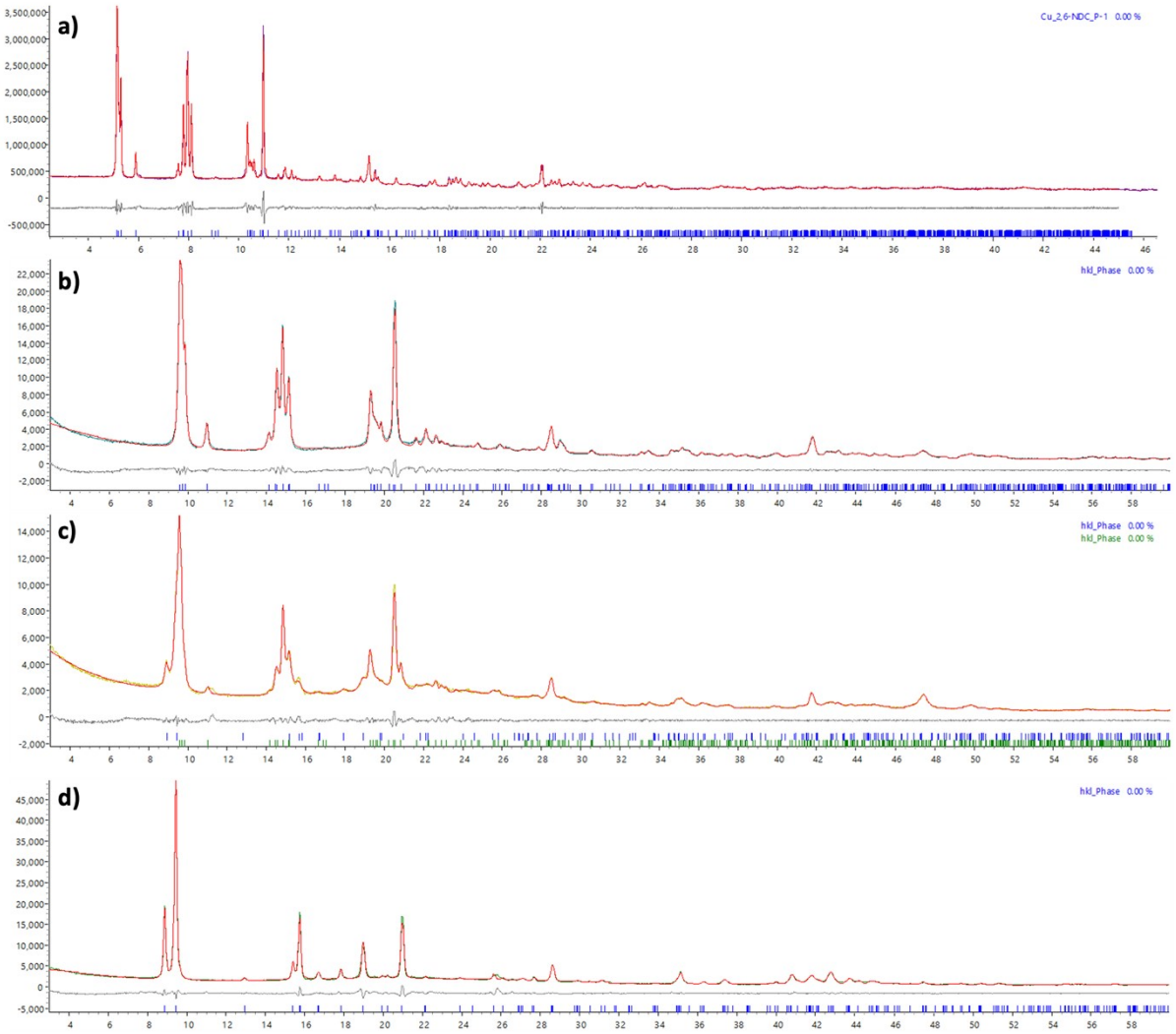

Figure S5. a-b) Pawley fit of PXRD data of as-synthesised **Cu(L2)** to a single phase with unit cell parameters consistent with the previously reported [Zn(L2)(lutidine)] phase (XOLZUT).[10] **a)** Synchrotron data. Pawley refinement, employing 1330 parameters (9 background, 1 zero error, 5 peak profile, 6 cell parameters and 1309 peaks). **b)** Laboratory Cu-Kα data. Pawley refinement, employing 467 parameters (9 background, 1 zero error, 5 peak profile, 6 cell parameters and 446 peaks). **c-d)** In house PXRD of the acetonitrile exchanged **Cu(L2)** fitted to comparable 2D coordination polymers ([Zn(L2)(lutidine)], XOLZUT and [Cu(L2)(pyridine)], XOMBAC).[10] **c)** Fitted as mixed phase, Pawley refinement, employing 703 parameters (9 background, 1 zero error, 9 peak profile, 10 cell parameters and 674 peaks).**d)** Fitted as a single phase, Pawley refinement, employing 247 parameters (9 background, 1 zero error, 5 peak profile, 4 cell parameters and 228 peaks).

Table S2. Unit cell parameters obtained from Pawley refinement shown in Figures S4a-e. Synchrotron radiation has a wavelength of 0.826581 Å.

	λ	**SG**	**Volume**	***a***	***b***	***c***	***α***	***β***	***γ***	***Rwp***	***Rwp'***
5a	Synch.	P-1	762.76(2)	8.0372 (1)	10.462 9(2)	10.636 3(2)	58.731 5(6)	87.094 0(7)	86.301 8(8)	0.0400	0.0577
5b	Cu Kα	P-1	765.3(1)	8.0520 (5)	10.471 3(7)	10.647 8(8)	58.702 (3)	87.061 (4)	86.213 (5)	0.0506	0.1037
5c	Cu Kα	P-1	765.7(2)	8.019(1)	10.499 (1)	10.659 (1)	58.781 (5)	87.125 (6)	86.268 (7)	0.0388	0.0449
		C2/m	1458.3(5)	10.699 (2)	19.759 (4)	6.943(1)	90	96.51(1)	90		
5d	Cu Kα	C2/m	1443.7(2)	10.639 0(7)	19.864 (1)	6.8614 (5)	90	95.380 (6)	90	0.0613	0.1339

Cu(L3)

To our knowledge, no solved structures for Cu(L3) are available and our attempts to grow single crystals large enough for structure analysis were unsuccessful.

A related structure, $Cu_2(BPDC)_2(Py)(MeOH)$ (where py is pyridine) was reported by Yaghi and co-workers in 2008 which form the expected 2D grid of paddle wheels, but is 2-fold interpenetrated.[12] Another related structure was reported in 2010 by Peng and co-workers which forms the expected layered structure with $[Cu_2L_2(DMF)_2]\cdot 6H_2O$, but where L= 3,3′-dimethoxy-4,4′-biphenyldicarboxylic acid.[13]

Wöll and coworkers[11] reported a series of 2D coordination polymers grown of surfaces (SURMOFs) consisting of a paddlewheel SBU and a series of dicarboxylates with increasing number of aromatic rings between the carboxylates, including Cu(L3). No prcessable data is available but their modelling indicated highly symmetrical *P*4-type stacking for Cu(L3), in which each Cu_2-PW stacks directly above and below those in adjacent layers. The synthetic conditions used in our are similar to those used by Wöll and our PXRD data (**Figure 1**) provide a good match to those reported by Wöll and coworkers.[11]

It is worth noting that, unlike the other two compounds, Cu(L3) shows no change in structure upon desolvation in acetonitrile. This is consistent Cu(L3) showing eclipsed stacking of layers of to give P4 symmetry which don't change on desolvation, in contrast to the off-set layers of Cu(L1) and Cu(L2).

The different behaviours of the three systems following solvent exchange are shown in Figure S6.

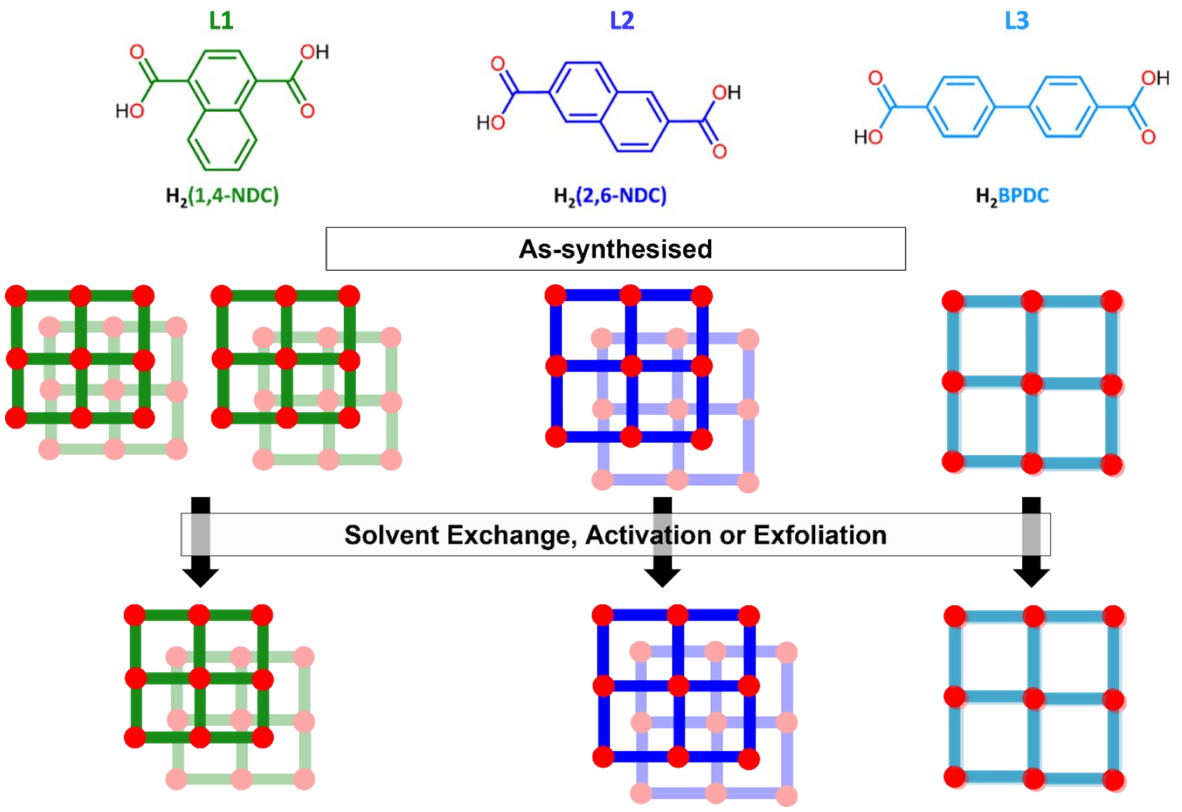

Figure S6. Summary image expressing the observations, from powder diffraction analysis (**Figure 1** and **Section S2**), that phase transformations can occur during synthesis as well as during the processing stages required to generate the desired nanosheets. Cu(L1) is synthesised as two phases with different layer offsets, which become single phase upon solvent exchange or exfoliation. Cu(L2) is synthesised a single phase, and the layer offsets then change upon exfoliation or activation. Cu(L3) is synthesised with no layer offset, and remains as such after any treatment.

To summarise, there is good evidence to support the formation of an isoreticular series of layered compounds with different lengthed linkers each forming Cu_2-PW units connected together with an **sql** topology. However, differences in linker length do result in subtle differences in the way the layers pack together, with Cu(L1) and Cu(L2) adopting staggered layers and Cu(L3) with eclipsed layers. This in turn affects how easily the samples desolvate under activation/exfoliation or solvent exchange (Figure S6). Whilst these differences in interlayer packing will affect the ease of sonication to a degree, they are a consequence of the differences in linker length so make a fair comparison. It is also unsurprising, and in fact desirable, that the layers of these materials appear able to slide over each other to occupy different positions with relative ease.

S3. Supplementary data for the layered MOF series

3.1 Images of reactions

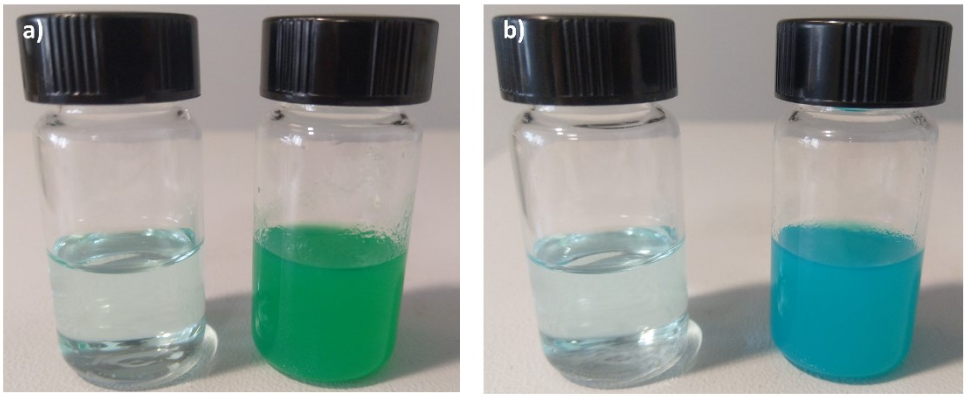

Figure S7. Images showing reaction solutions for the synthesis of **a)** Cu(L1) and **b)** Cu(L2) from nitrate (left) and acetate (right) salts approximately 20 seconds after mixing.

3.2 NMR Spectroscopy

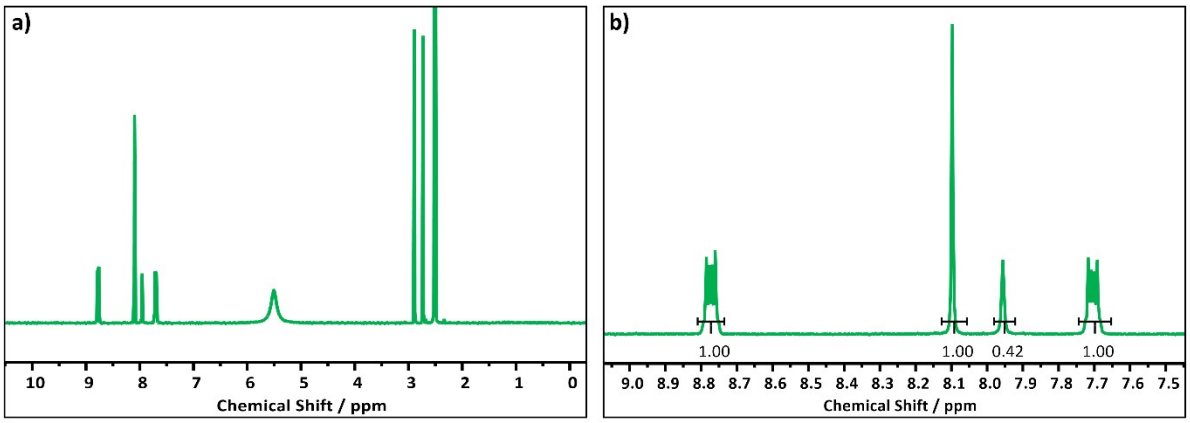

Figures S8. ^{1}H NMR spectra of the Cu(L1) MOF synthesised from the nitrate salt, digested in DCl and d_6-DMSO, showing **a)** the full spectrum and **b)** a focus on the linker region.

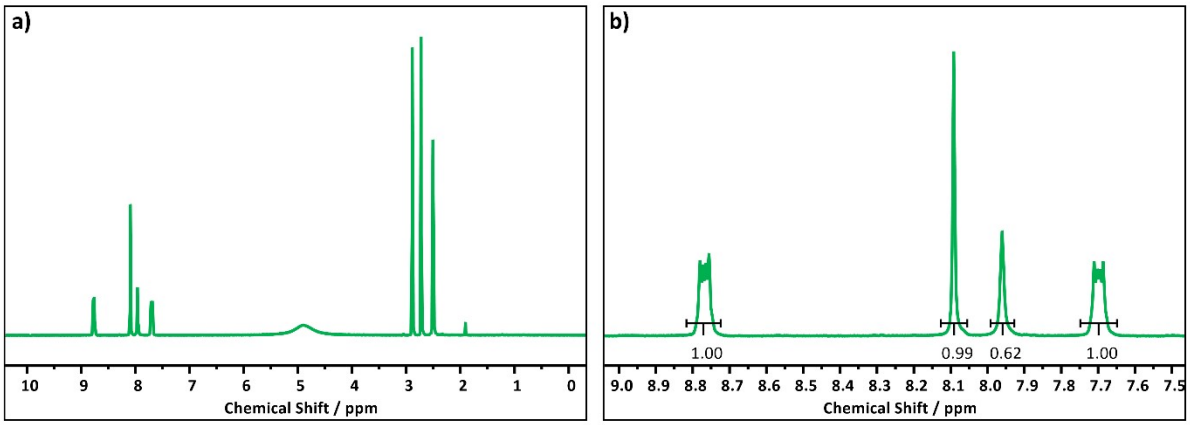

Figures S9. ^{1}H NMR spectra of the Cu(L1) MOF synthesised from the acetate salt, digested in DCl and d_6-DMSO, showing **a)** the full spectrum and **b)** a focus on the linker region.

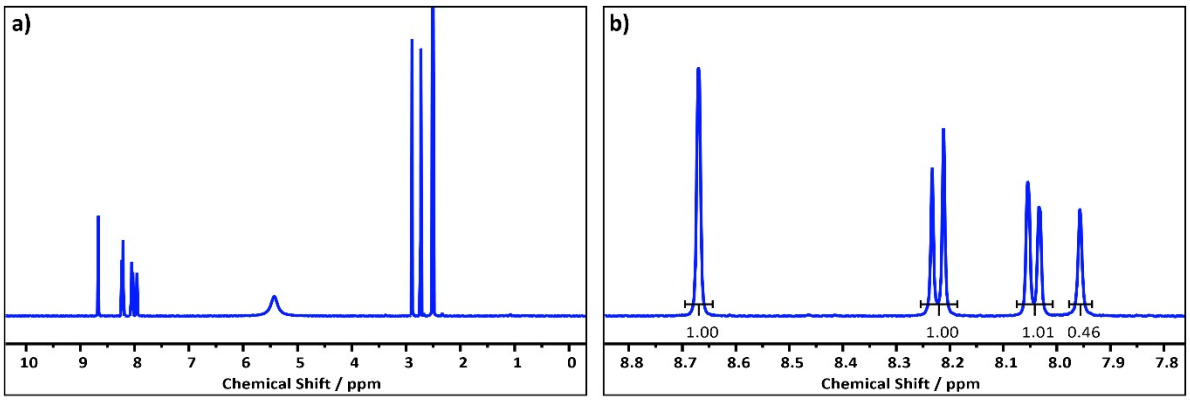

Figures S10. ^{1}H NMR spectra of the Cu(L2) MOF synthesised from the nitrate salt, digested in DCl and d_6-DMSO, showing **a)** the full spectrum and **b)** a focus on the linker region.

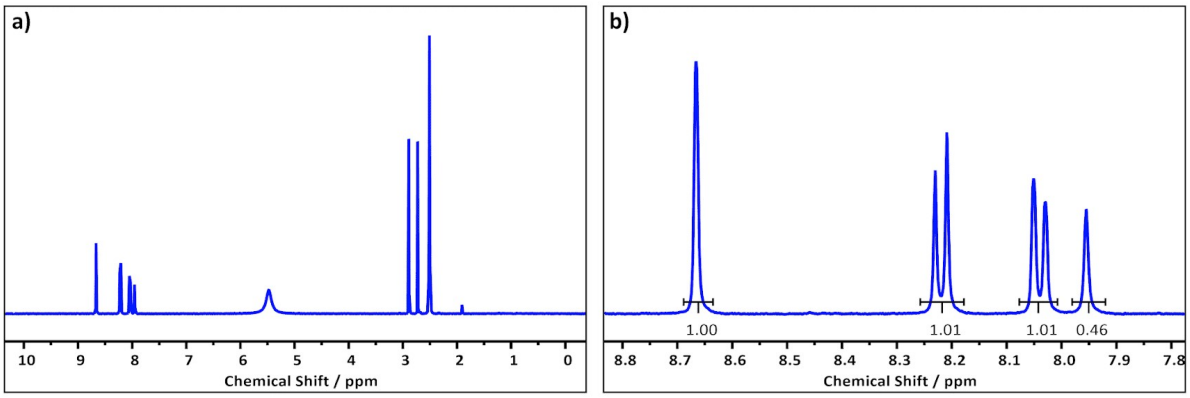

Figures S11. ^{1}H NMR spectra of the Cu(L2) MOF synthesised from the acetate salt, digested in DCl and d_6-DMSO, showing **a)** the full spectrum and **b)** a focus on the linker region.

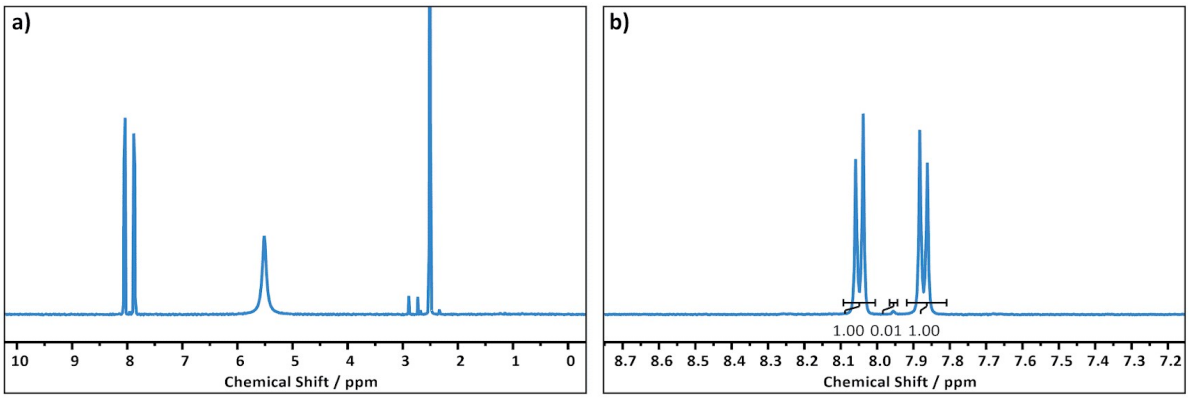

Figures S12. ^{1}H NMR spectra of the Cu(L3) MOF synthesised from the nitrate salt, digested in DCl and d_6-DMSO, showing **a)** the full spectrum and **b)** a focus on the linker region.

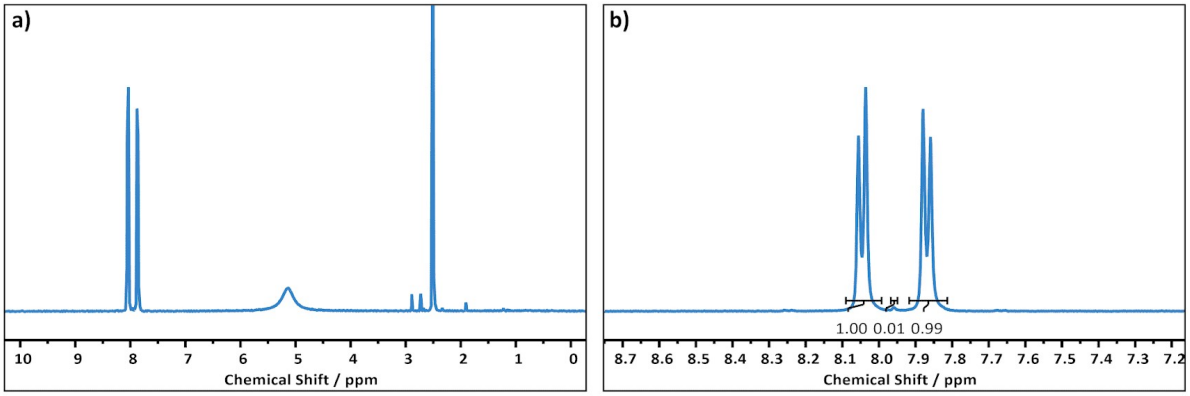

Figures S13. ^{1}H NMR spectra of the Cu(L3) MOF synthesised from the acetate salt, digested in DCl and d_6-DMSO, showing **a)** the full spectrum and **b)** a focus on the linker region.

3.3 Elemental Analysis

Table S3. Elemental microanalysis data for all layered MOFs prepared in this study. Measurements are determined to a tolerance of ± 0.5%, with differences between the calculated percentages and the observed percentages shown as Δ.

Cu(L1) synthesised from nitrate salt				
	Observed	**Calc. $CuC_{15}H_{13}NO_5$**	**Calc. $CuC_{14.52}H_{12.88}N_{0.84}O_{5.34}$***	**Δ**
C	49.91	51.35	50.09	-0.18
H	3.94	3.73	3.70	+0.24
N	3.35	3.99	3.38	-0.03

* Accounting for 0.84 DMF and 0.5 water solvation

Cu(L1) synthesised from acetate salt				
	Observed	**Calc. $CuC_{15}H_{13}NO_5$**	**Calc. $CuC_{15.88}H_{15.97}N_{1.26}O_{5.86}$***	**Δ**
C	49.97	51.35	49.96	+0.01
H	4.25	3.73	4.19	+0.06
N	4.52	3.99	4.62	-0.10

* Accounting for 1.26 DMF solvation, 0.5 water solvation and 0.05 acetate inclusion

Cu(L2) synthesised from nitrate salt				
	Observed	**Calc. $CuC_{15}H_{13}NO_5$**	**Calc. $CuC_{14.76}H_{12.44}N_{0.92}O_{4.92}$***	**Δ**
C	51.37	51.35	51.39	-0.02
H	3.86	3.73	3.61	+0.25
N	3.83	3.99	3.74	-0.09

* Accounting for 0.92 solvation

Cu(L2) synthesised from acetate salt				
	Observed	**Calc. $CuC_{15}H_{13}NO_5$**	**Calc. $CuC_{15.78}H_{14.82}O_{5.26}N_{1.26}$***	**Δ**
C	51.10	51.35	51.32	-0.22
H	3.98	3.73	3.62	+0.36
N	3.93	3.99	3.71	+0.22

* Accounting for 0.92 solvation and 0.04 acetate inclusion

Cu(L3) synthesised from nitrate salt				
	Observed	**Calc. $CuC_{14}H_8O_4$**	**Calc. $CuC_{14}H_{10}O_5$***	**Δ**

C	51.70	55.37	52.26	-0.56
H	3.52	2.65	3.13	+0.39
N	0.00	0.00	0.00	0.00

* Accounting for 1 equivalent water

Cu(L3) synthesised from acetate salt				
	Observed	**Calc. $CuC_{14}H_8O_4$**	**Calc. $CuC_{14.06}H_{10.09}NO_{5.06}$***	**Δ**
C	51.84	55.37	52.19	-0.35
H	3.44	2.65	3.12	+0.32
N	0.00	0.00	0.00	0.00

* Accounting for 1 equivalent water and 0.03 acetate inclusion

3.4 Thermogravimetric Analysis

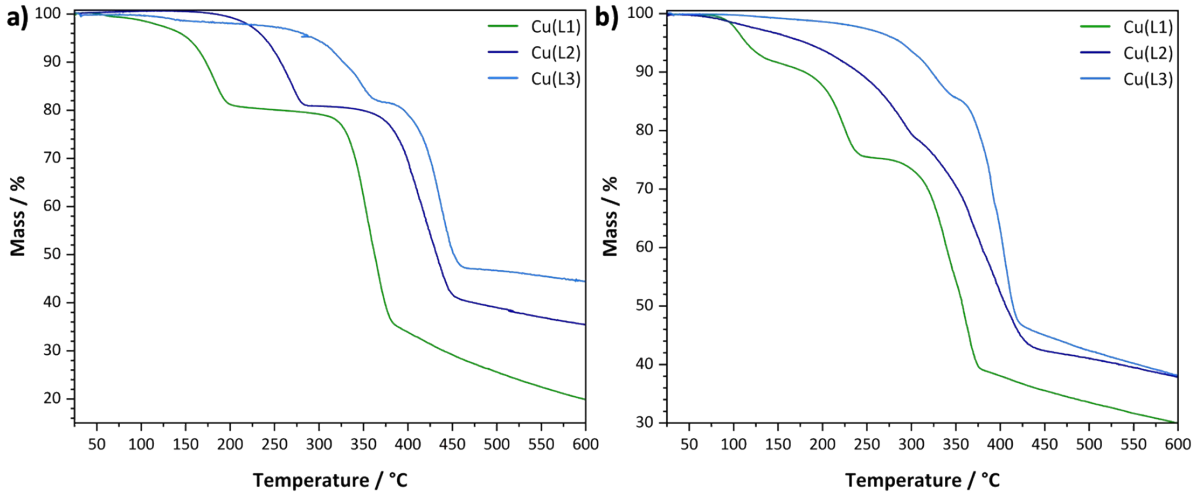

Figure S14. TGA profiles for the layered MOFs synthesised from **a)** the nitrate salt and **b)** the acetate salt.

3.5 Infrared Spectroscopy

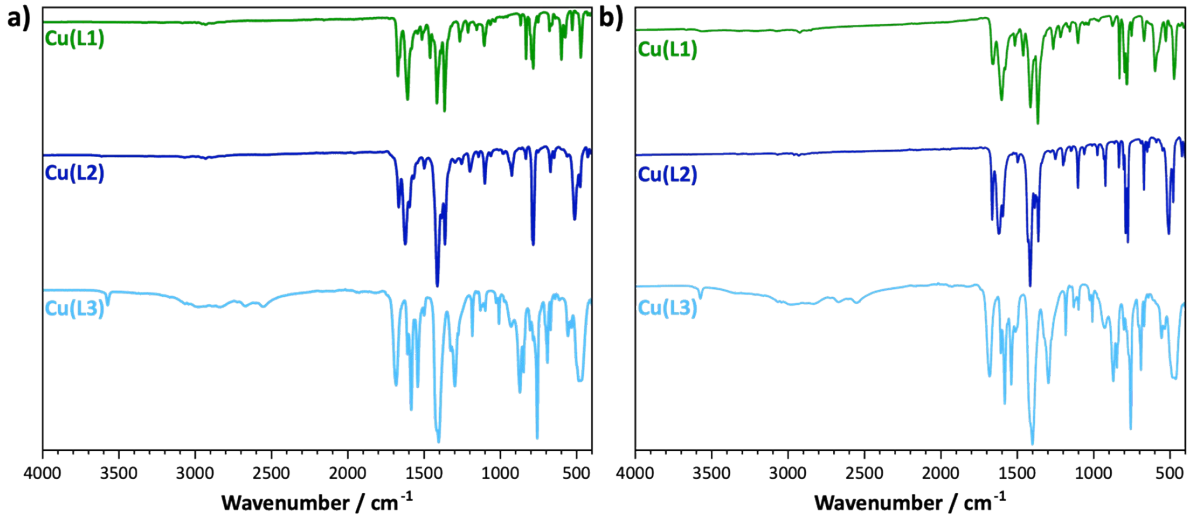

Figure S15. FT-IR spectra for the layered MOFs as-synthesised from **a)** the nitrate salt and **b)** the acetate salt.

3.6 Electron microscopy

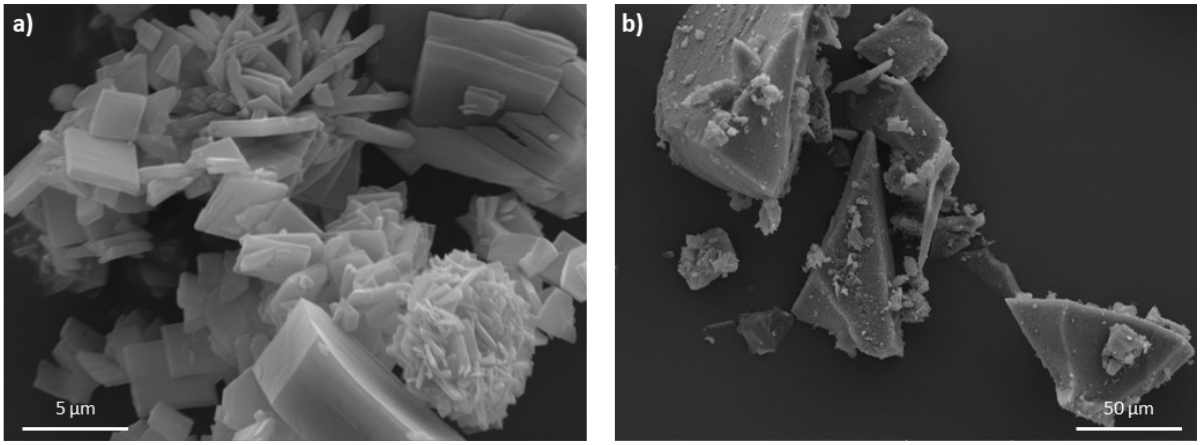

Figure S16. SEM images of as-synthesised Cu(L1) formed from **a)** the nitrate and **b)** the acetate salt.

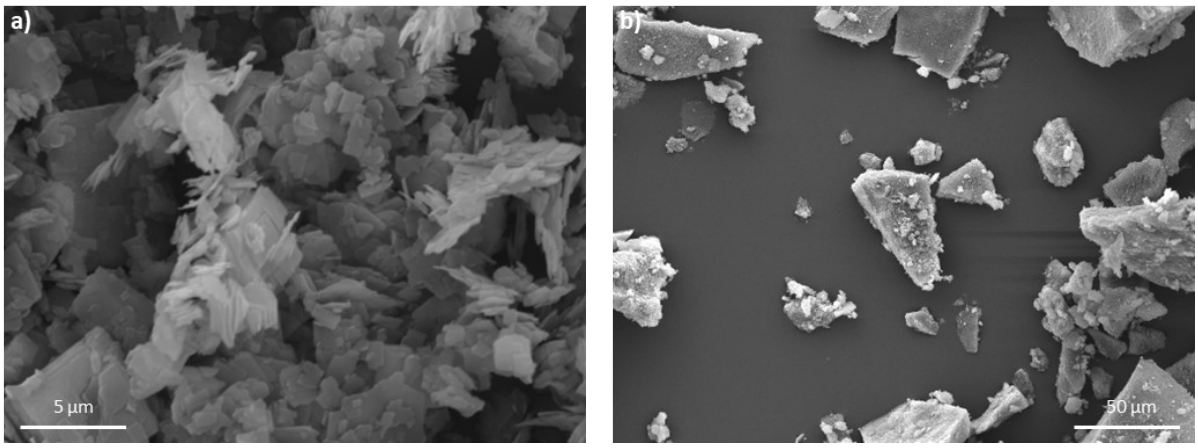

Figure S17. SEM images of as-synthesised Cu(L2) formed from **a)** the nitrate and **b)** the acetate salt.

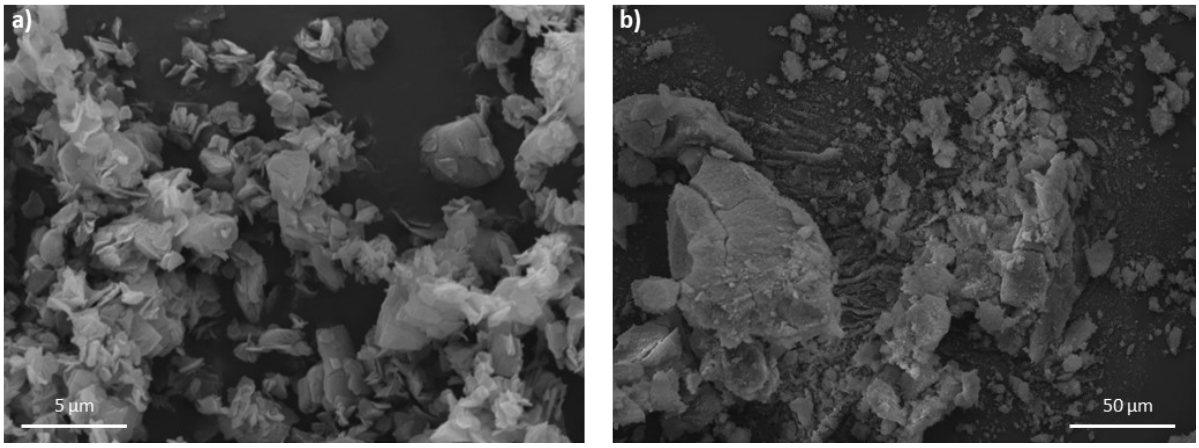

Figure S18. SEM images of as-synthesised Cu(L3) formed from **a)** the nitrate and **b)** the acetate salt.

S4. Supplementary data for the desolvated layered MOF series

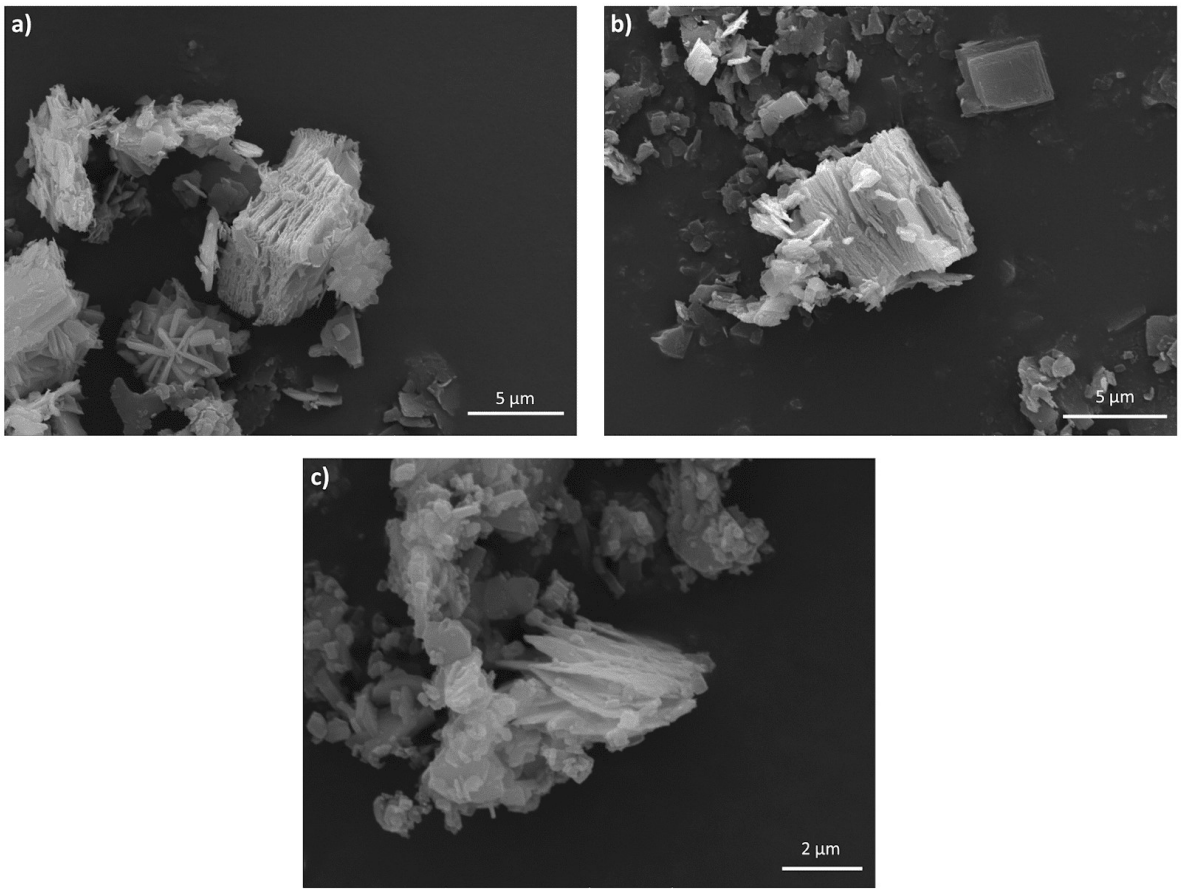

Figure S19. SEM images of the layered MOFs desolvated in acetonitrile: **a)** Cu(L1), **b)** Cu(L2) and **c)** Cu(L3). Note that while the axial sites of the Cu(L3) paddlewheel are already desolvated after synthesis, the MOF was subject to the same procedure to examine any effects on structure or morphology.

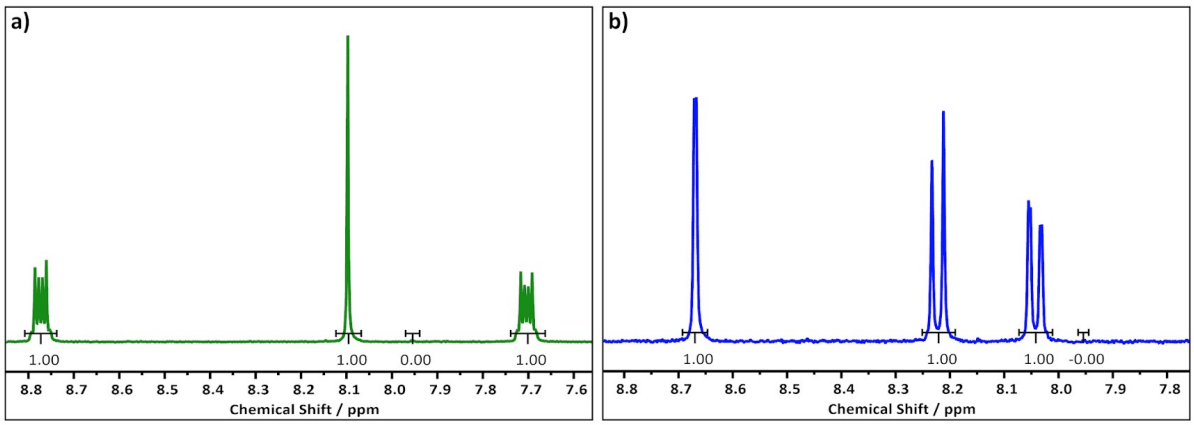

Figures S20. ^{1}H NMR spectra of desolvated **a)** Cu(L1) and **b)** Cu(L2) digested in DCl and d_6-DMSO. Integration of the 7.95 ppm region indicates full desolvation.

S5. Supplementary data for the exfoliated MON series

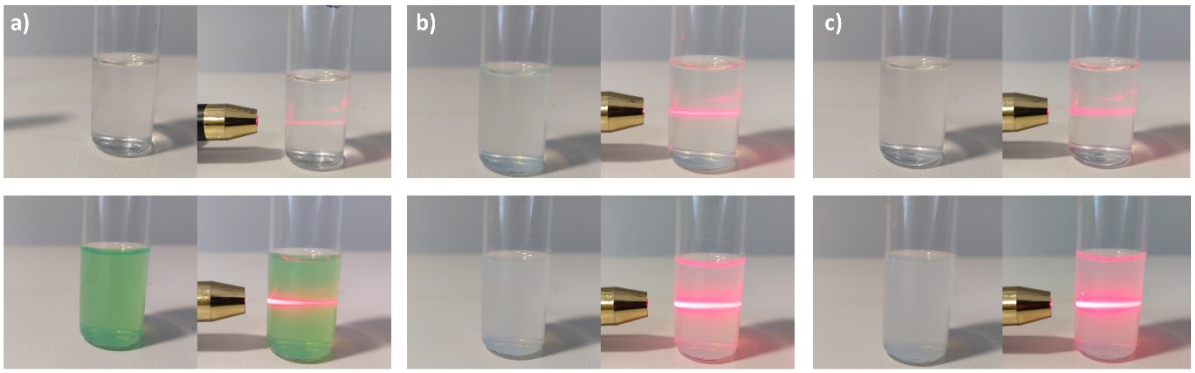

Figure S21. Images of suspensions and Tyndall scattering of MONs obtained from the nitrate salt (top) and the acetate salt (bottom) for **a)** Cu(L1), **b)** Cu(L2) and **c)** Cu(L3).

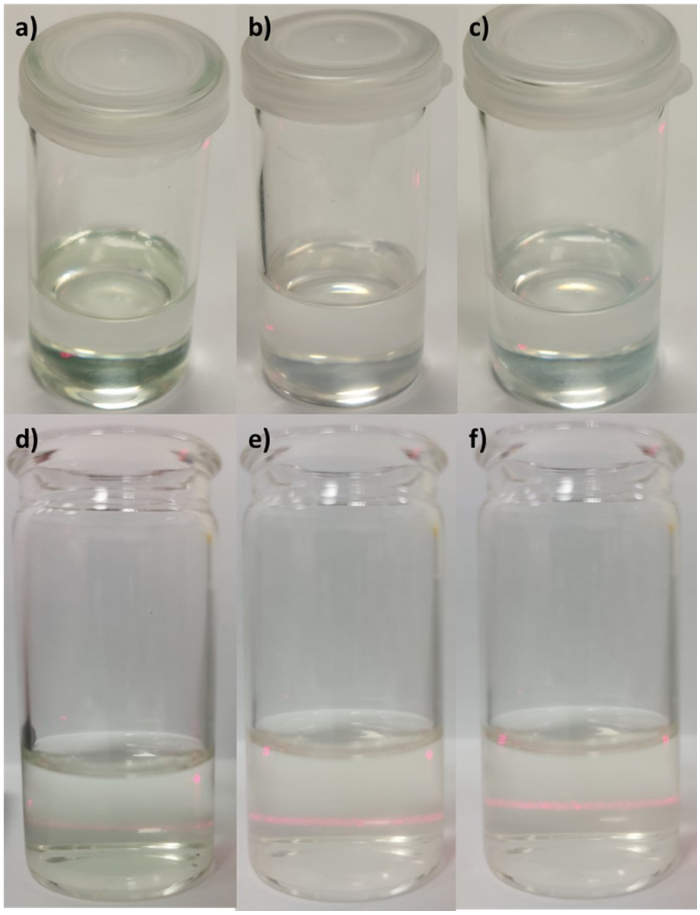

Figure S22. Images of suspensions of **a)** Cu(L1), **b)** Cu(L2), and **c)** Cu(L3) MONs obtained from the nitrate salt after aggregation and crashing out after 3 days, shown alongside images after resuspension *via* 30 seconds of sonication in **d)**-**f)**. Note that in the crashed out aggregated samples, no Tyndall scattering is observed, whereas Tyndall scattering can be clearly observed after resuspension.

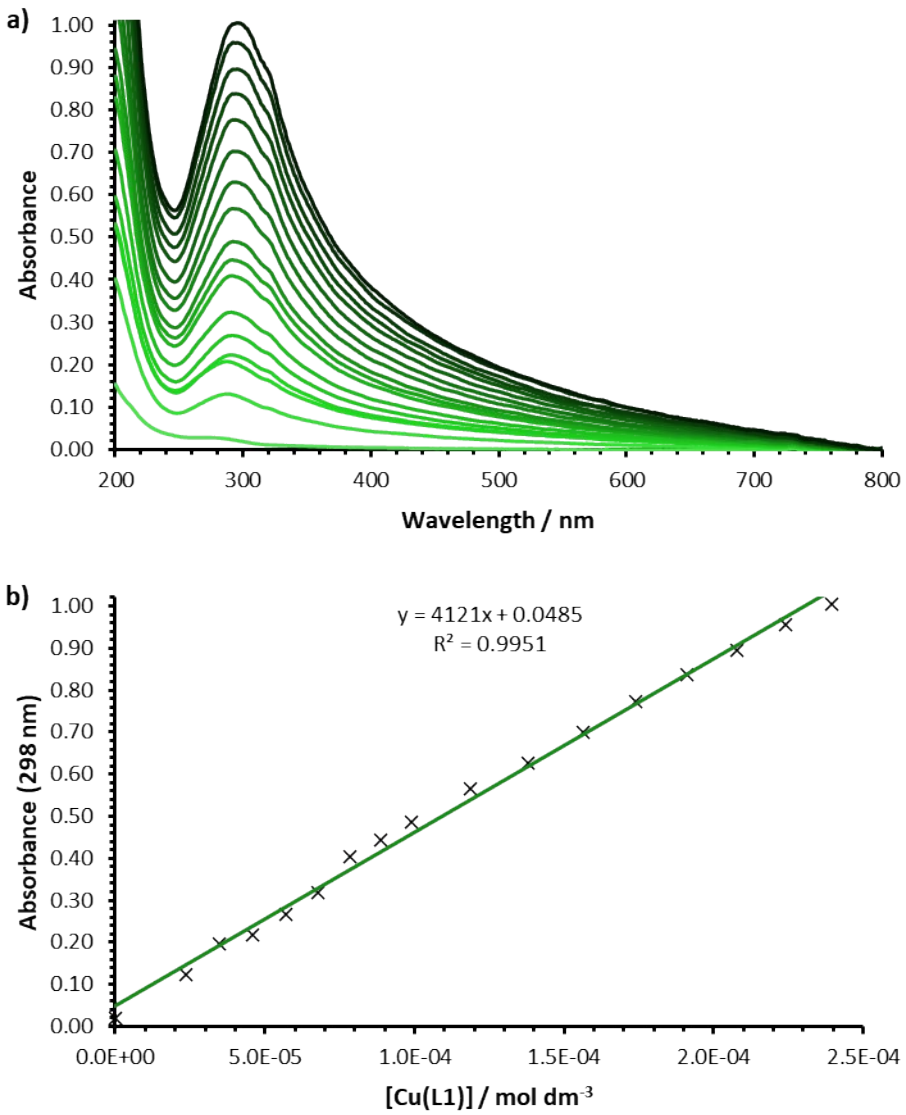

Figure S23. a) UV-visible spectra and **b)** line plots used to determination the extinction coefficient of Cu(L1) at λ_{max} = 298 nm.

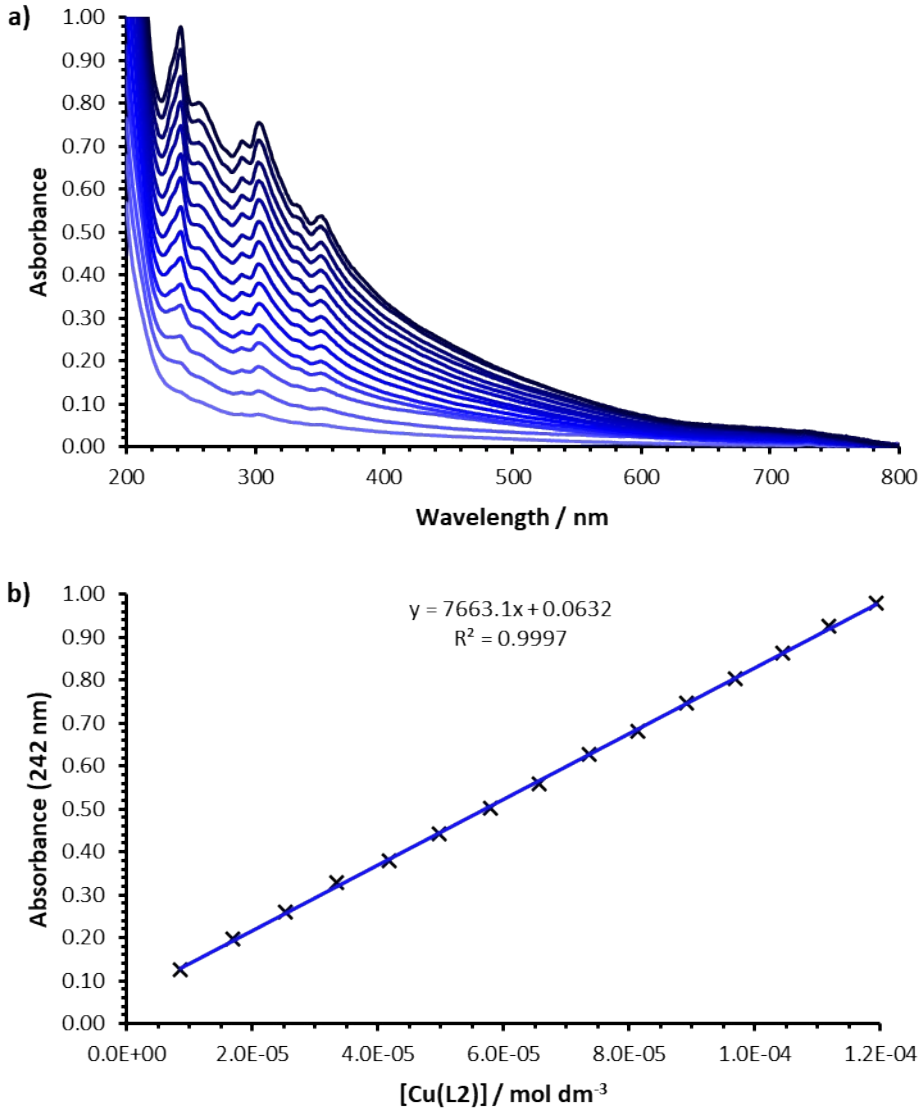

Figure S24. a) UV-visible spectra and **b)** line plots used to determination the extinction coefficient of Cu(L2) at λ_{max} = 242 nm.

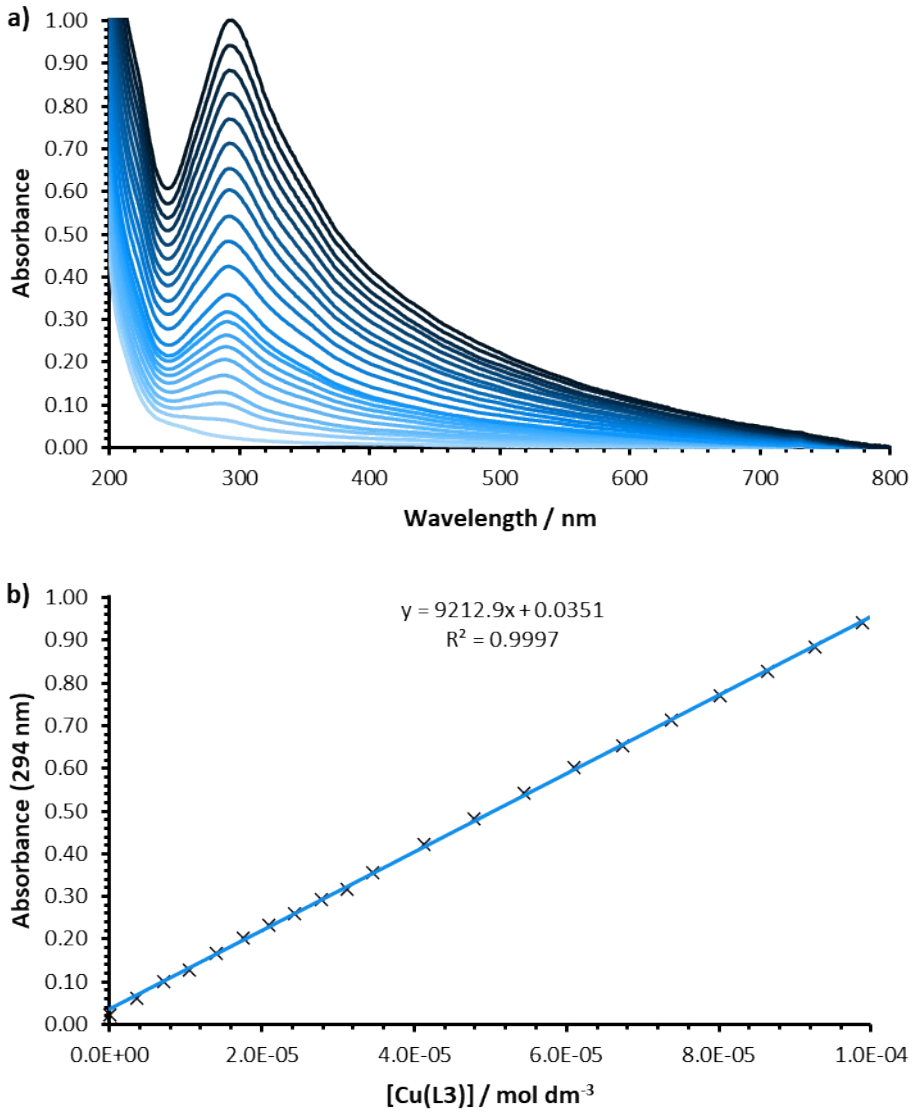

Figure S25. a) UV-visible spectra and **b)** line plots used to determination the extinction coefficient of Cu(L3) at λ_{max} = 294 nm.

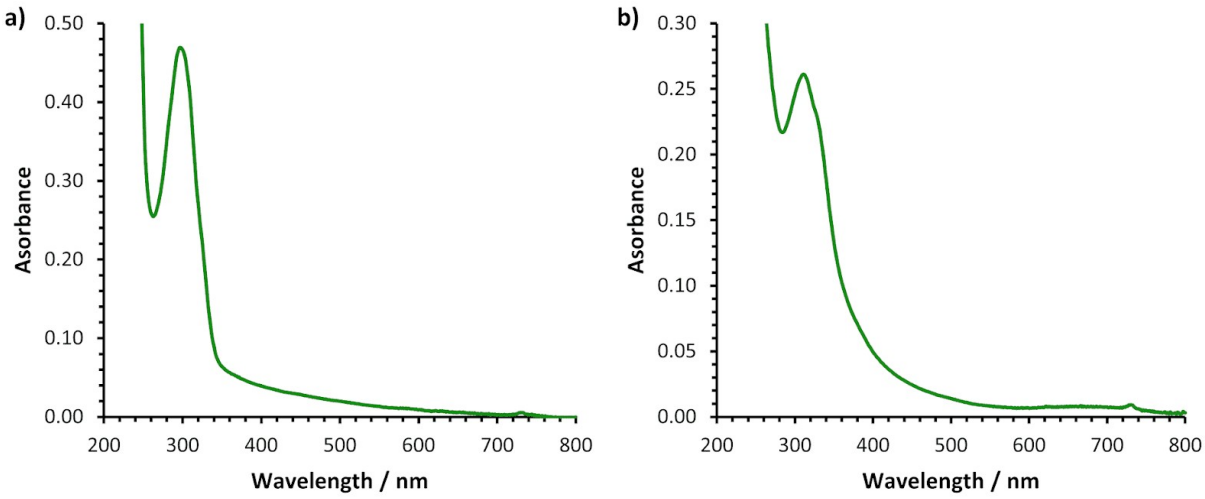

Figure S26. UV-visible absorption spectra used to determine concentrations of suspensions of Cu(L1) MON synthesised from the **a)** nitrate and **b)** acetate salt.

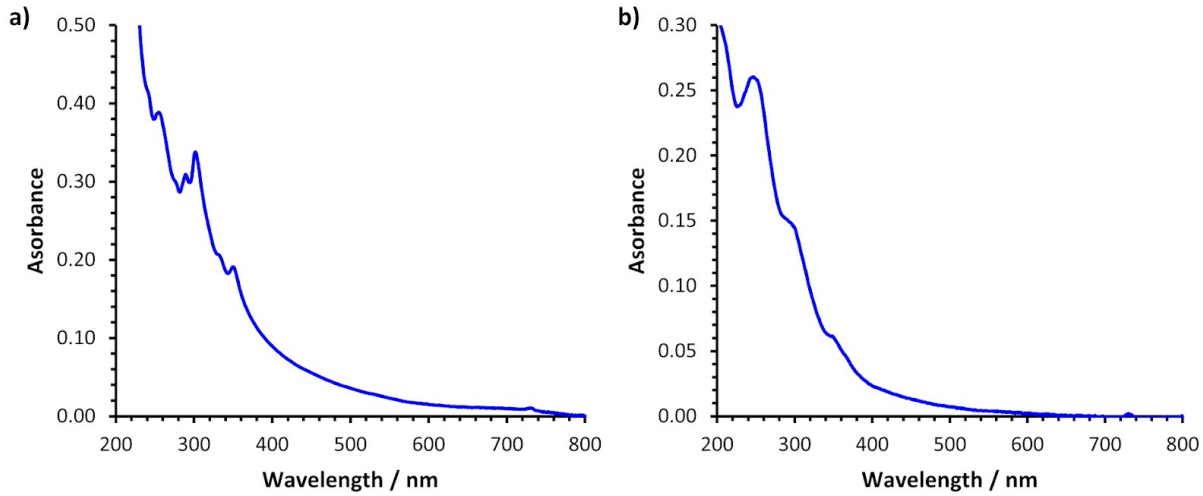

Figure S27. UV-visible absorption spectra used to determine concentrations of suspensions of Cu(L2) MON synthesised from the **a)** nitrate and **b)** acetate salt.

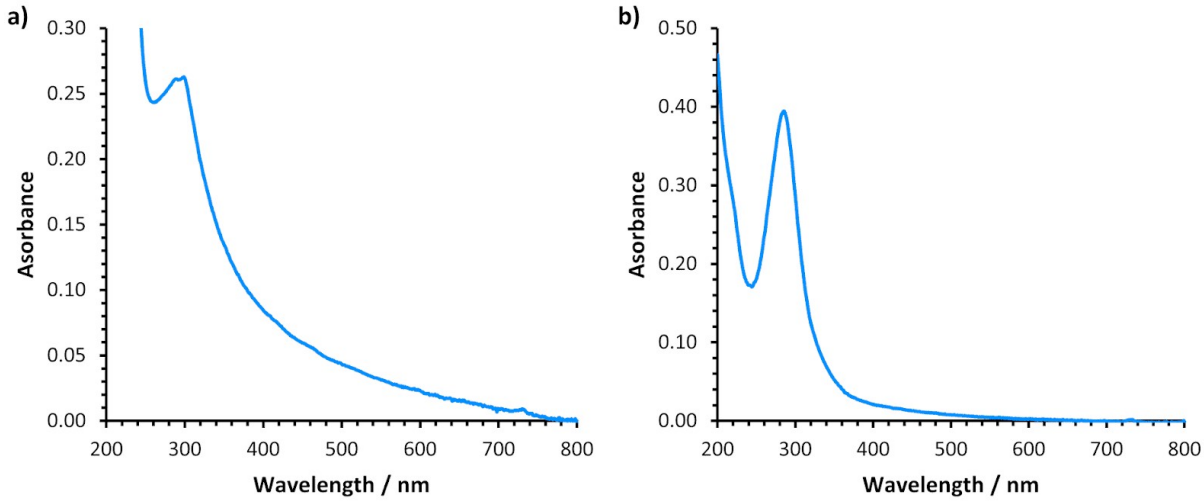

Figure S28. UV-visible absorption spectra used to determine concentrations of suspensions of Cu(L3) MON synthesised from the **a)** nitrate and **b)** acetate salt.

Table S4. Concentrations of MON suspensions as determined from the UV-Vis spectra in Figures S19-21.

	Cu(L1)		**Cu(L2)**		**Cu(L3)**	
Conc. / mg mL^{-1}	**Nitrate**	**Acetate**	**Nitrate**	**Acetate**	**Nitrate**	**Acetate**
	0.1	0.7	0.1	0.6	0.05	0.7

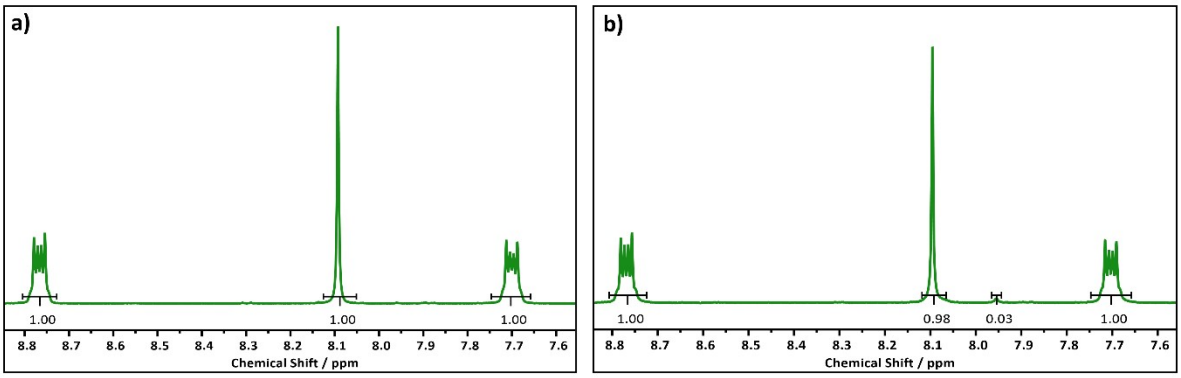

Figures S29. ^{1}H NMR spectra of the material obtained from centrifugation after exfoliation of Cu(L1 materials synthesised from the **a)** nitrate and **b)** acetate salts.

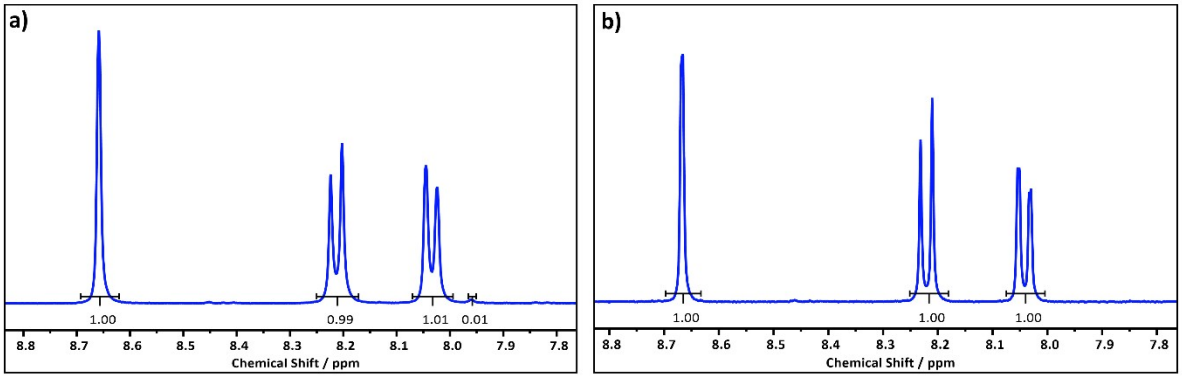

Figures S30. ^{1}H NMR spectra of the material obtained from centrifugation after exfoliation of Cu(L2 materials synthesised from the **a)** nitrate and **b)** acetate salts.

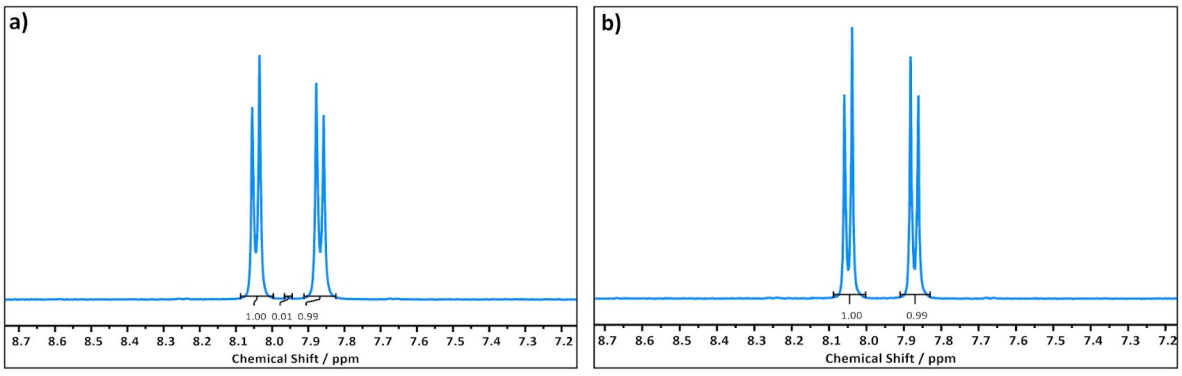

Figures S31. ^{1}H NMR spectra of the material obtained from centrifugation after exfoliation of Cu(L3) materials synthesised from the **a)** nitrate and **b)** acetate salts.

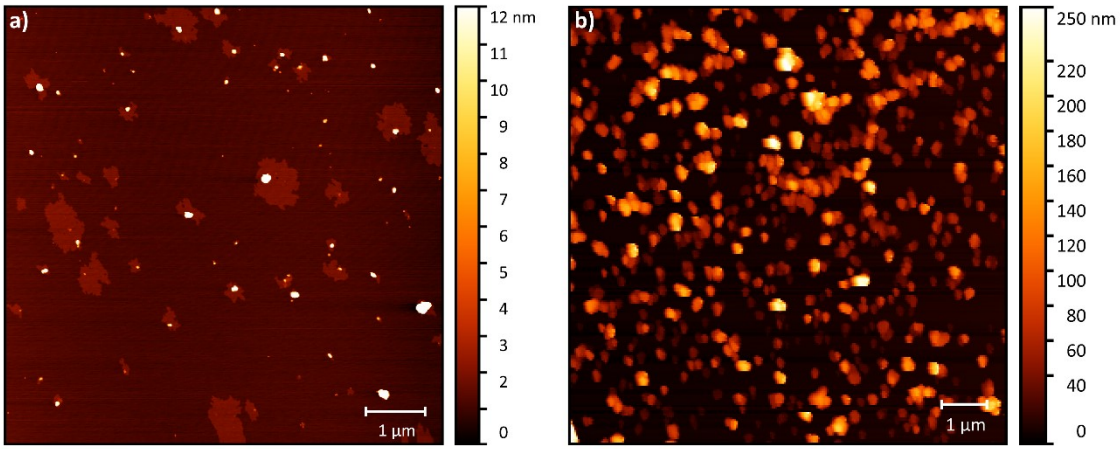

Figure S32. Supplementary AFM images of Cu(L1) MONs synthesised from the **a)** nitrate and **b)** acetate salt.

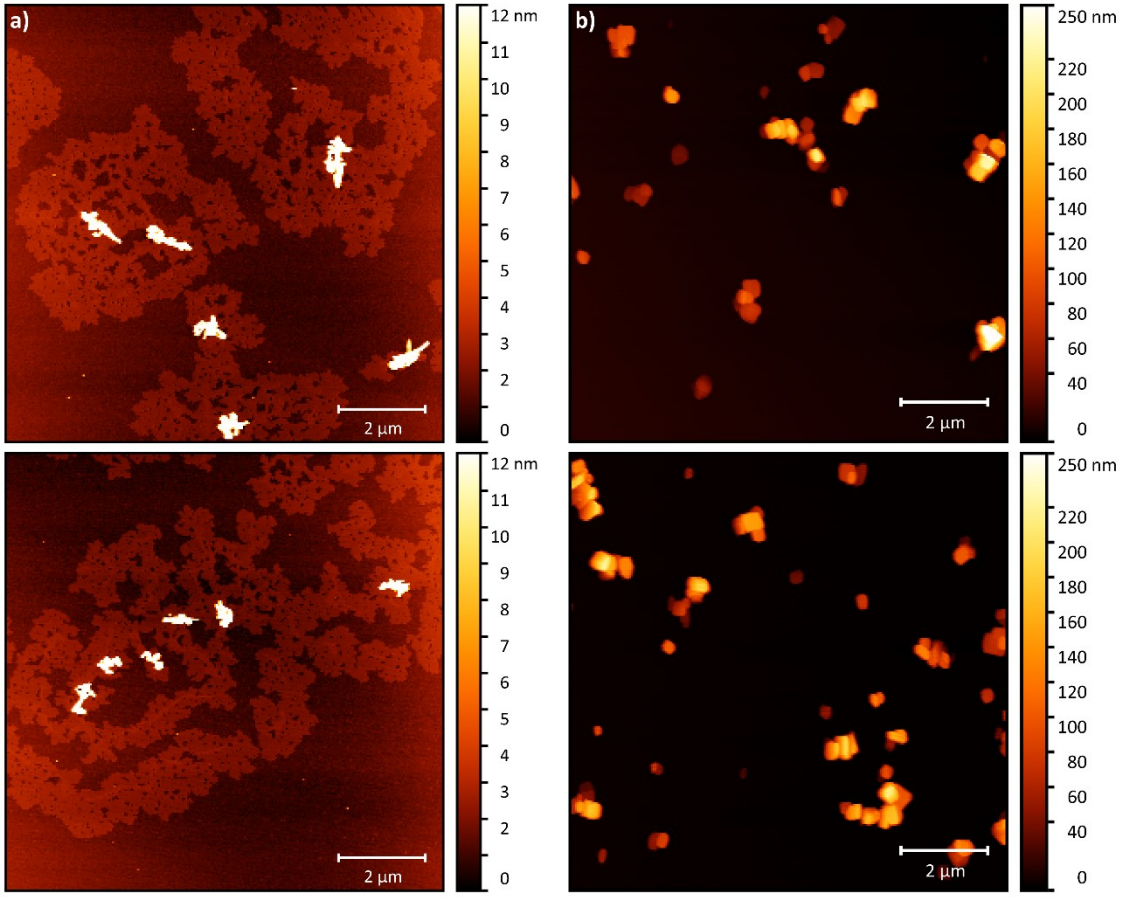

Figure S33. Supplementary AFM images of Cu(L2) MONs synthesised from the **a)** nitrate and **b)** acetate salt.

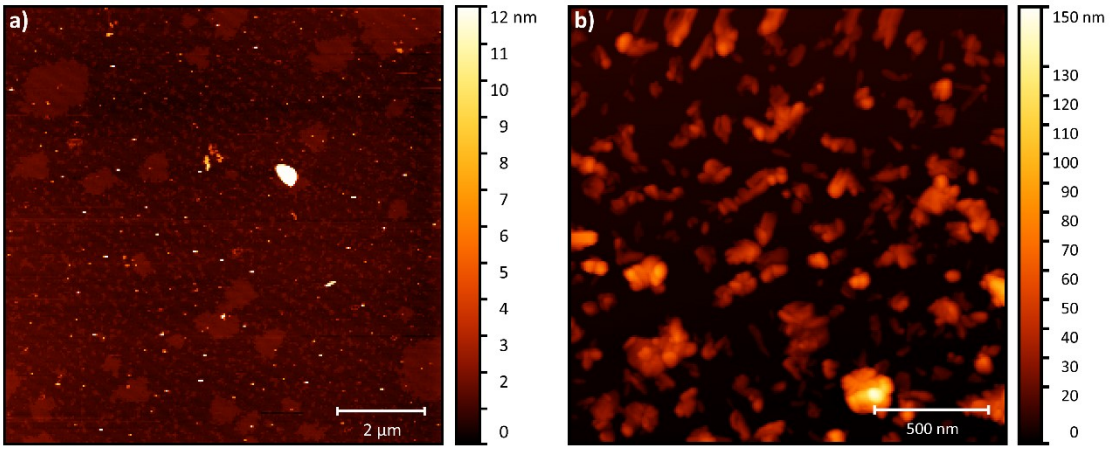

Figure S34. Supplementary AFM images of Cu(L3) MONs synthesised from the **a)** nitrate and **b)** acetate salt.

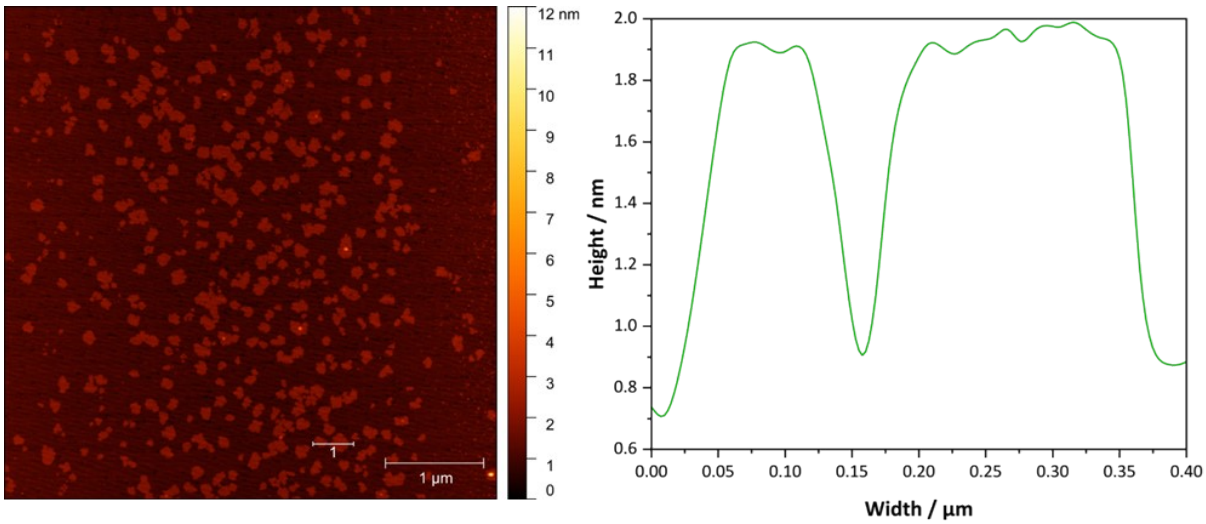

Figure S35. AFM image of Cu(L1) MONs obtained from the nitrate series with a representative height profile.

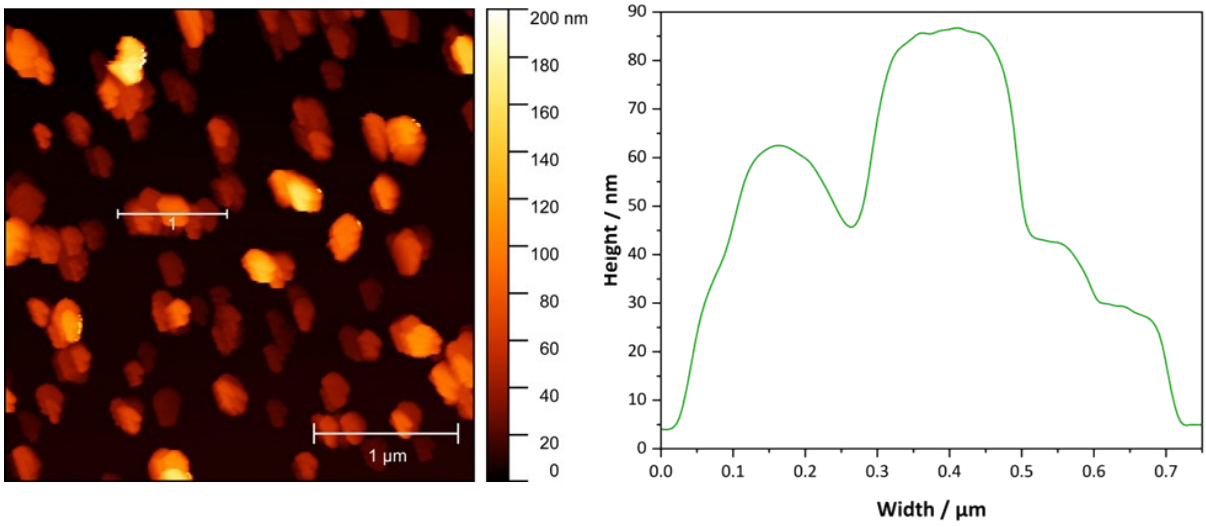

Figure S36. AFM image of Cu(L1) MONs obtained from the acetate series with a representative height profile.

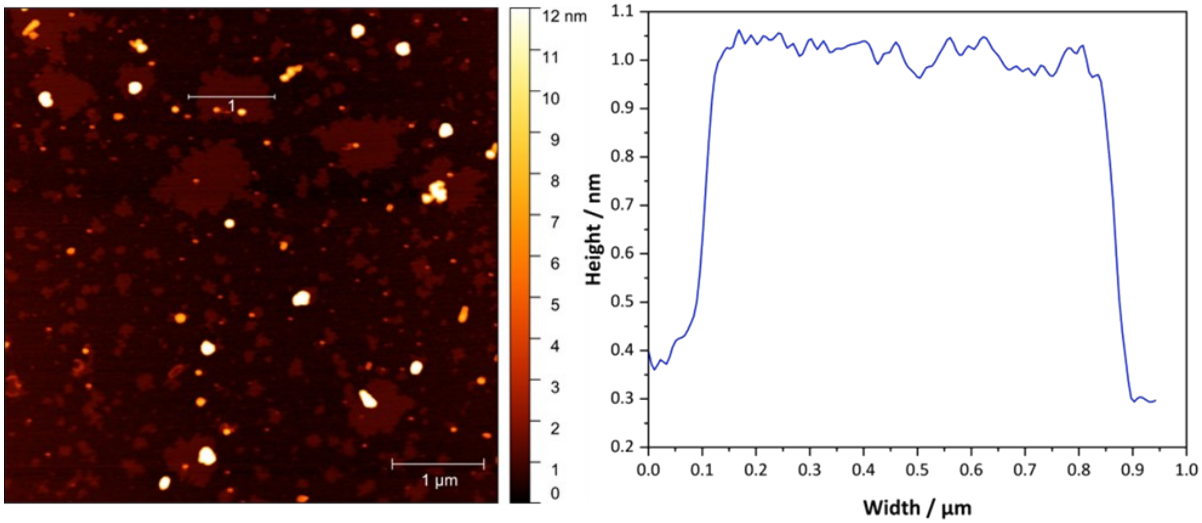

Figure S37. AFM image of Cu(L2) MONs obtained from the nitrate series with a representative height profile.

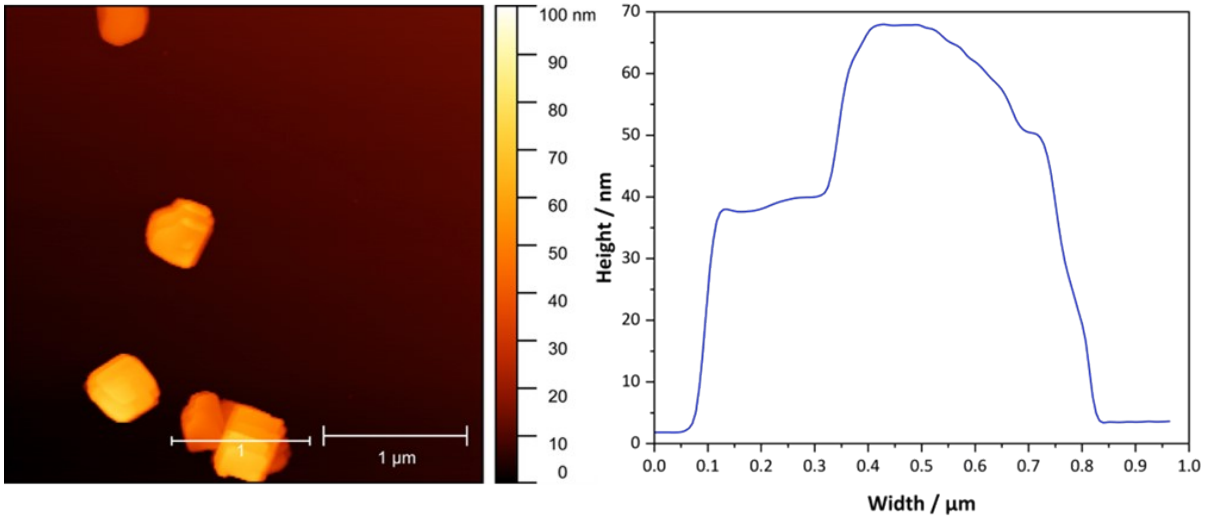

Figure S38. AFM image of Cu(L2) MONs obtained from the acetate series with a representative height profile.

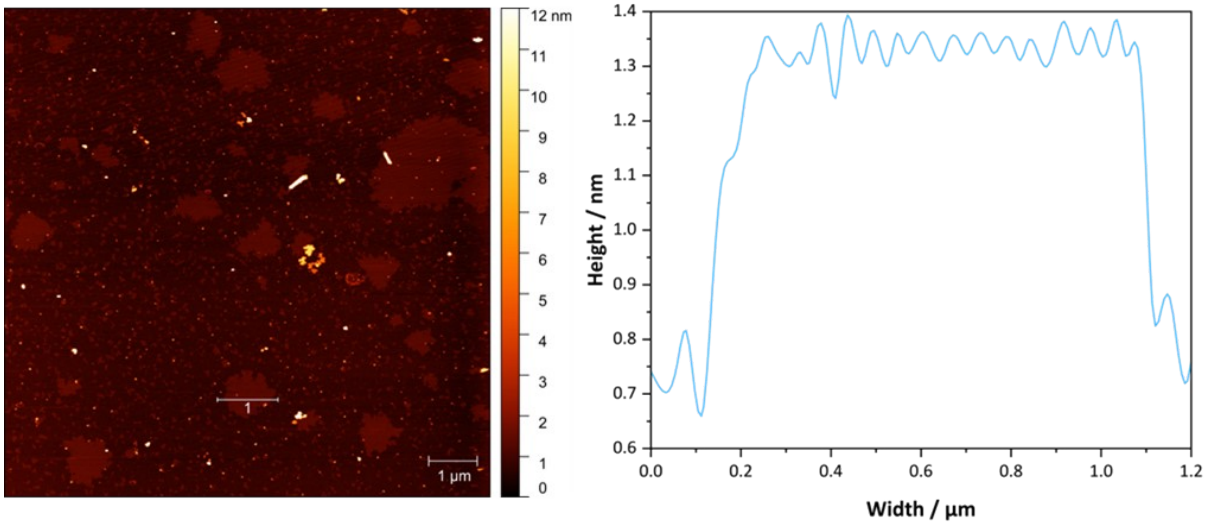

Figure S39. AFM image of Cu(L3) MONs obtained from the nitrate series with a representative height profile.

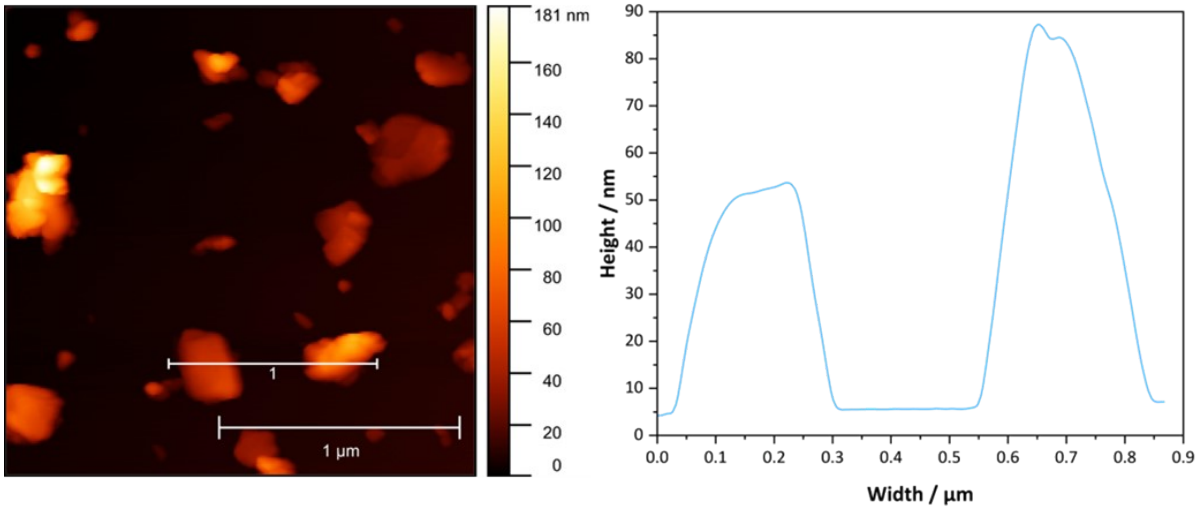

Figure S40. AFM image of Cu(L3) MONs obtained from the acetate series with a representative height profile.

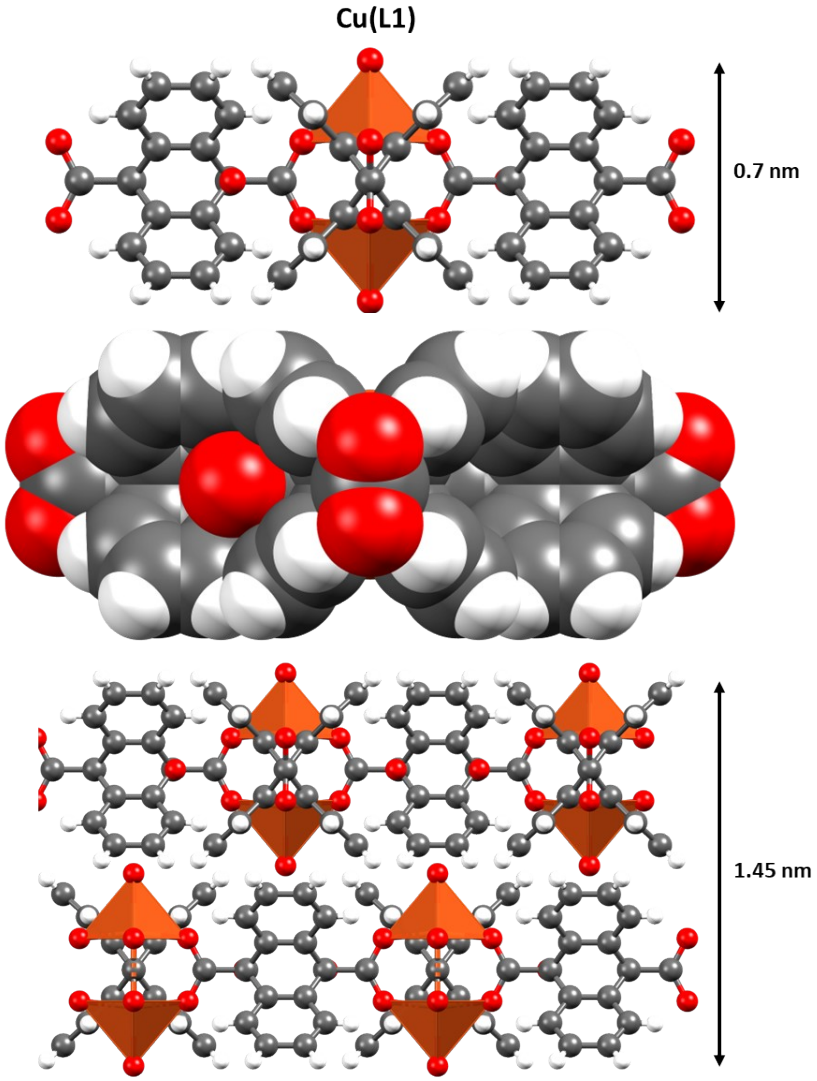

Figure S41. Crystallographic dimensions of the Cu(L1) system, indicating a layer thickness of 0.70 nm for a monolayer and 1.45 nm for a bilayer. A spacefill representation of the monolayer is also shown to consider the effect of van der Waals radii on the monolayer thickness.

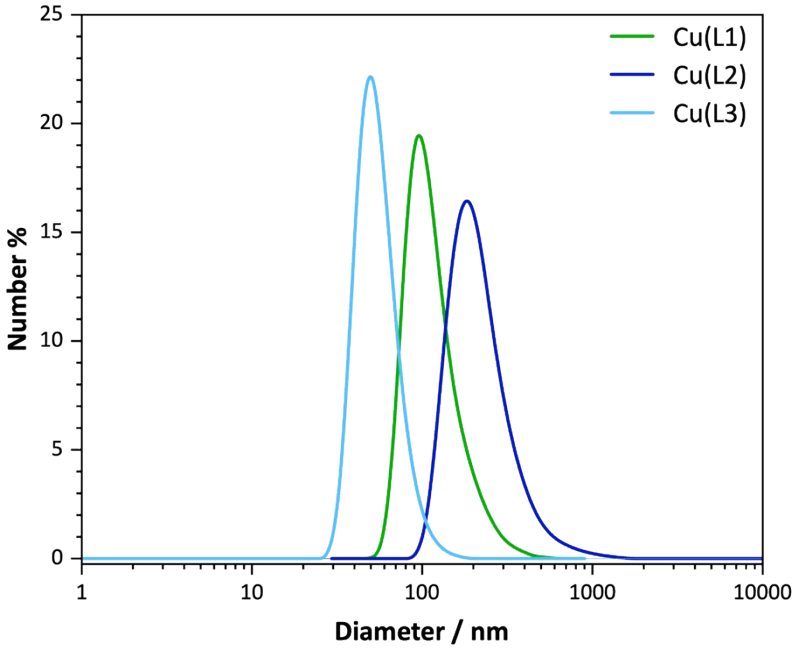

Figure S42. DLS number plot for MON suspensions of Cu(L1), Cu(L2) and Cu(L3) formed from the acetate salt. Suspensions were each diluted by a factor of 10 before analysis.

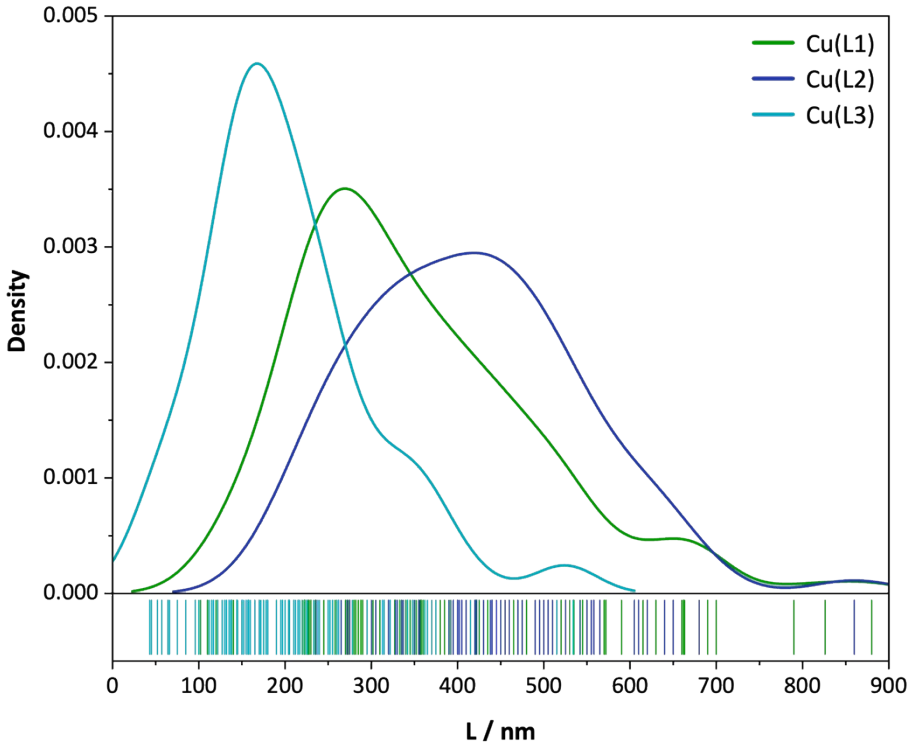

Figure S43. Density distribution profiles of nanosheet lateral dimensions for MONs synthesised from the acetate salt obtained from AFM imaging data.

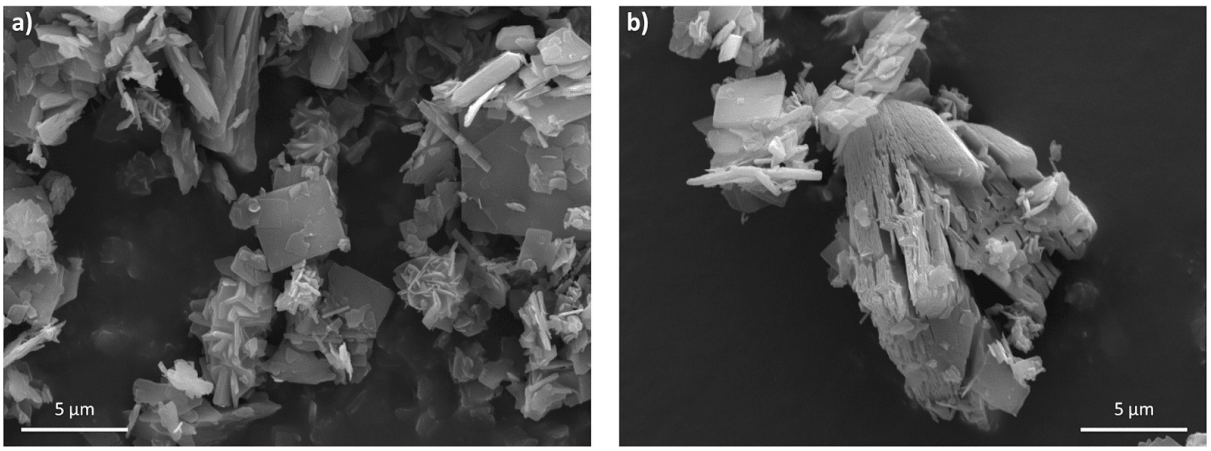

Figure S44. SEM images of post-exfoliation bulk material of Cu(L1) synthesised from the nitrate salt.

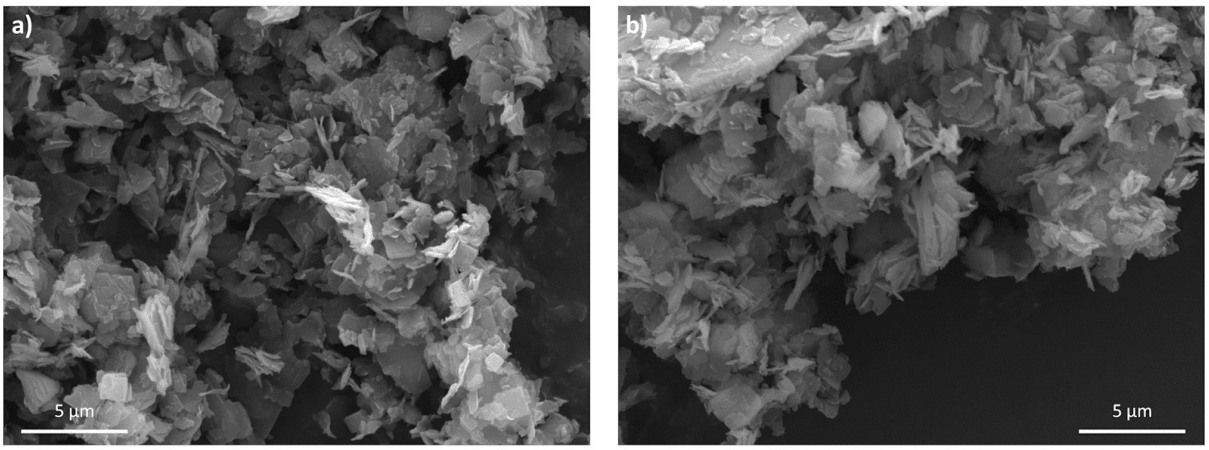

Figure S45. SEM images of post-exfoliation bulk material of Cu(L2) synthesised from the nitrate salt.

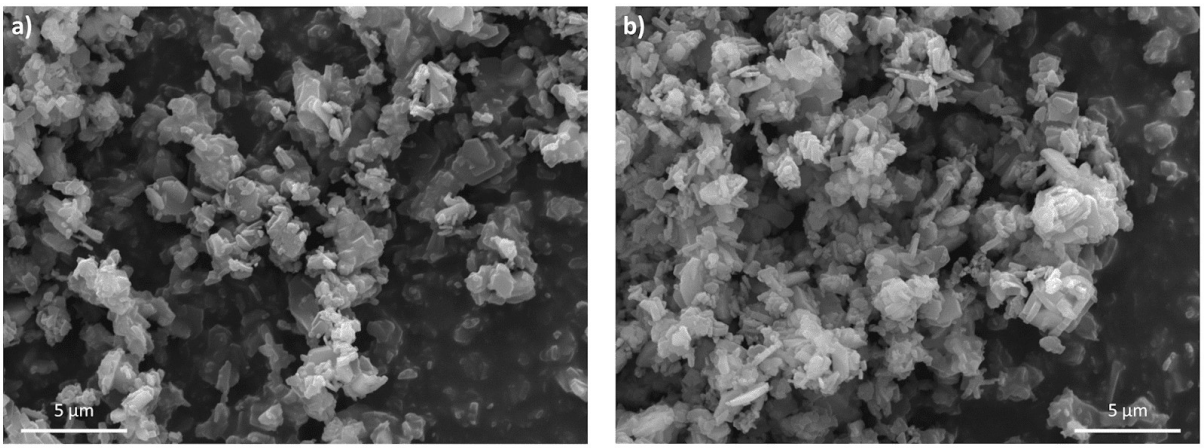

Figure S46. SEM images of post-exfoliation bulk material of Cu(L3) synthesised from the nitrate salt.

S6. References

1 S. P. Thompson, J. E. Parker, J. Potter, T. P. Hill, A. Birt, T. M. Cobb, F. Yuan and C. C. Tang, *Rev. Sci. Instrum.*, 2009, **80**, 075107.

2 S. P. Thompson, J. E. Parker, J. Marchal, J. Potter, A. Birt, F. Yuan, R. D. Fearn, A. R. Lennie, S. R. Street and C. C. Tang, *J. Synchrotron Radiat*, 2011, **18**, 637-648.

3 P. Kanoo, K. L. Gurunatha and T. K. Maji, *J. Mater. Chem.*, 2010, **20**, 1322–1331.

4 G. S. Pawley, *J. Appl. Crystallogr.*, 1981, **14**, 357–361.

5 A. A. Coelho, *Topas Acad. Version 6,see http//www.topas-academic.net*.

6 A. A. Coelho, J. Evans, I. Evans, A. Kern and S. Parsons, *Powder Diffr.*, 2011, **26**, S22–S25.

7 A. A. Coelho, *J. Appl. Cryst.,* 2018, **51**, 210-218.

8 M. Eddaoudi, J. Kim, D. Vodak, A. Sudik, J. Wachter, M. O'Keeffe and O. M. Yaghi, *Proc. Natl. Acad. Sci. U. S. A.*, 2002, **99**, 4900–4904.

9 F. Shahangi Shirazi and K. Akhbari, *Inorganica Chim. Acta*, 2015, **436**, 1–6.

10 K. O. Kongshaug and H. Fjellvåg, *J. Solid State Chem.*, 2002, **166**, 213–218.

11 J. Liu, B. Lukose, O. Shekhah, H. K. Arslan, P. Weidler, H. Gliemann, S. Bräse, S. Grosjean, A. Godt, X. Feng, K. Müllen, I. B. Magdau, T. Heine and C. Wöll, *Sci. Rep.*, 2012, **2**, 1–5.

12 H. Furukawa, J. Kim, N. W. Ockwig, M. O'Keeffe, O. M. Yaghi, J. Am. Chem. Soc., 2008, 130, 11650–11661

13 X. Wang, D. Zhu, Y. Xu, J. Yang, X. Shen, J. Zhou, N. Fei, X. Ke, L. Peng, *Cryst. Growth Des.* 2010, 10, 2, 887−894